Modeling Basin- and Plume-Scale Processes of CO_2 Storage for Full-Scale Deployment

Quanlin Zhou *[a], Jens T. Birkholzer [a],

Edward Mehnert [b], Yu-Feng Lin [c], Keni Zhang [a]

*corresponding author, Email: QZhou@lbl.gov, Tel: 510-486-5748, Fax: 510-486-5686,
Address: MS 90-1116, One Cyclotron Road

[a] Earth Sciences Division, Lawrence Berkeley National Laboratory, University of California,
Berkeley, CA 94720

[b] Illinois State Geological Survey, Champaign, IL 61820

[c] Illinois State Water Survey, Champaign, IL 61820

Abstract

Integrated modeling of basin- and plume-scale processes induced by full-scale deployment of CO_2 storage was applied to the Mt. Simon aquifer in the Illinois Basin. A 3D mesh was generated with local refinement around 20 injection sites, with ~30 km spacing. A total annual injection rate of 100 Mt CO_2 over 50 years was employed. The CO_2-brine flow at the plume scale and the single-phase flow at the basin scale were simulated. Simulation results show the overall shape of a CO_2 plume consisting of a typical *gravity-override subplume* in the bottom injection zone of high injectivity and a *pyramid-shaped subplume* in the overlying multilayered Mt. Simon, indicating the important role of a secondary seal with relatively low permeability and high entry capillary pressure. The secondary seal effect is manifested by retarded upward CO_2 migration as a result of multiple secondary seals, coupled with lateral preferential CO_2 viscous fingering through high-permeability layers. The plume width varies from 9.0 to 13.5 km at 200 years, indicating the slow CO_2 migration and no plume interference between storage sites. On the basin scale, pressure perturbations propagate quickly away from injection centers, interfere after less than a year, and eventually reach basin margins. The simulated pressure buildup of 35 bar in the injection area is not expected to affect caprock geomechanical integrity. Moderate pressure buildup is observed in Mt. Simon in northern Illinois. However, its impact on groundwater resources is less than the hydraulic drawdown induced by long-term extensive pumping from overlying freshwater aquifers.

1. Introduction

Geologic carbon sequestration (GCS) has been investigated for two decades as an effective measure for mitigating climate change—by storing CO_2 in oil and gas reservoirs, uneconomic coal seams, and deep saline aquifers (Steinberg 1992; Van der Meer 1992; Bachu et al. 1994; Pruess and Garcia 2002; IPCC 2005). Various small-scale GCS projects have been or are currently being conducted in the world (e.g., Hovorka et al. 2006). Two industrial-scale projects have (for years) been in operation in deep saline aquifers at the Sleipner site in the North Sea and at the In Salah site in Algeria, and more large-scale demonstration projects are in the planning stages within the United States (USDOE 2008) and other countries. The main objective of these projects is to demonstrate, directly or indirectly, the safe containment of injected CO_2 in storage formations, through extensive field monitoring (e.g., Arts et al. 2004; Daley et al. 2008), sampling and analysis (e.g., Freifeld et al. 2005), and comprehensive numerical modeling and calibration (e.g., Bickle et al. 2007; Doughty et al. 2008). Most of the research has focused on the migration and trapping of CO_2 in storage formations, and on potential leakage into shallow aquifers and the atmosphere through leaky pathways. The scale for the region occupied by free-phase CO_2 at a single industrial-scale injection site is referred to here as the "plume scale", which is typically on the order of less than 100 km^2. Much less effort has been devoted to studying transport phenomena of resident fluids (i.e., brine in saline aquifers) at a scale of sedimentary basins. Here, this scale is referred to as the "basin scale", which can be on the order of several 100,000 km^2.

Basin-scale phenomena may become particularly important when multiple injection sites are used for full-scale deployment of GCS within an individual basin. This injection and storage scenario will occur if GCS, as a mature and cost-effective technology, is fully employed to effectively reduce atmospheric emissions of CO_2 as part of an effort to mitigate climate change. Recently, Zhou et al. (2008) and Birkholzer et al. (2009) investigated basin-scale pressure buildup and brine migration (in addition to the plume-scale processes) caused by industrial-scale CO_2 storage at a single project site in idealized aquifer-seal systems, with a focus on a variety of sensitivity analyses. Yamamoto et al. (2009) simulated the large-scale pressure buildup and brine migration in response to a storage scenario of 10 Mt (million metric tones) CO_2 per year at ten injection sites in the Tokyo Bay; their solutions were significantly biased by the fixed-pressure conditions specified on the lateral boundaries of a limited model domain (60 km by 70 km). Nicot (2008) evaluated the pressure buildup and its hydrological impacts for a GCS scenario in the Texas Gulf Coast Basin, by using a traditional single-phase flow model with equivalent injection volume of resident brine. However, the single-phase flow model neglects the two-phase flow regime near each injection site, and thus cannot be used to address the plume-scale phenomena and caprock integrity. The caprock integrity mainly depends on (1) the fluid-pressure buildup in the two-phase flow regime within the storage formation and the seal's maximum tolerable pressure gradients, to avoid caprock fracturing (USEPA 1994); and (2) free-phase CO_2 buoyancy and height, as well as the seal's entry capillary pressure, to avoid CO_2 leakage (Schowalter 1979).

In this research, we focus on both plume- and basin-scale flow and transport processes caused by full-scale deployment of GCS at multiple sites in a storage formation of multiple alternating high- and low-permeability layers. For the plume-scale processes, we investigate the secondary seal effect (i.e., the effect of CO_2 accumulation under, penetration into, and breakthrough from an intra-storage-formation layer of relatively low permeability and higher entry capillary pressure, in comparison to its underlying and overlying layers) on retardation of upward CO_2 migration. We also explore pressure interference between different injection sites at an intermediate scale, as well as basin-scale pressure buildup, brine migration and leakage, and potential environmental impacts. We use, as an example, the Illinois Basin, which has extensive site characterization data and the potential for accommodating an infrastructure for full-scale deployment of GCS. We develop an integrated model, covering a core injection area in the center of the basin, where 20 individual storage sites are located, and a far-field area, where regional-scale pressure impacts can be expected. Possible implications of basin-scale pressure buildup on storage-capacity estimation and GCS regulation are discussed in Birkholzer and Zhou (2009).

2. Site Description of the Illinois Basin

The Illinois Basin is a deep sedimentary basin bounded by arches and domes, encompassing most of Illinois, southwestern Indiana, and western Kentucky (see Figure 1). The estimated total storage capacity is in the range of 31,000 to 124,000 Mt CO_2, including a storage capacity of 27,000 to 109,000 Mt CO_2 in the deep Mt. Simon Sandstone (USDOE 2008). The Midwest Geological Sequestration Consortium (MGSC) is preparing a large-scale demonstration project, the Illinois Basin–Decatur Project, at the Archer Daniels Midland (ADM) site in Decatur, Illinois, with an annual rate of 0.36 Mt CO_2 injected into the Mt. Simon Sandstone (henceforth referred to as Mt. Simon) for three years (2010 to 2013). This project, if successful, will help to demonstrate the feasibility of full-scale GCS, and may provide momentum for building a sound deployment infrastructure in the Illinois Basin. An area in the center of the basin was identified by MGSC researchers as an area in which many future storage sites would likely be located. This area, outlined in Figure 1, is referred to as the core injection area.

We focus on Mt. Simon as the primary storage formation, the overlying Eau Claire Shale (henceforth referred to as Eau Claire) as the regional seal, and the upper portion of Precambrian granite as the baserock. Our study benefits from the extensive investigations on natural gas storage fields in the basin (Buschbach and Bond 1974; Morse and Leetaru 2005) and on groundwater development in northern and central Illinois and southern Wisconsin (Visocky et al. 1985; Young 1992a, b; Feinstein et al. 2005). From these investigations, we collected various data needed for developing the integrated model to simulate the basin- and plume-scale processes in response to multi-site CO_2 storage.

2.1. Basin Geology

The geologic model for Mt. Simon and Eau Claire was developed using boreholes into Mt. Simon, some of which penetrate into the underlying Precambrian granite (Buschbach and Kolata 1991). The top elevation of Mt. Simon varies significantly from -4300 m above mean sea level (msl) in the south to -80 m msl in the north, corresponding to an average updip slope of about 8 m per kilometer. In the northern area, the relatively shallow Mt. Simon contains fresh groundwater, which was used for water supply in northeastern Illinois until the 1970s. The top of Mt. Simon is elevated to the eastern and western sides of the basin. As shown in Figure 2a, the formation is continuous throughout the entire basin, except in the southern and southwestern parts where Precambrian highs exist and Cambrian sediments are absent. The thickness of Mt. Simon varies significantly, from zero in the south to approximately 800 m in the bowl-shaped area farther north. In the core injection area, the Mt. Simon thickness varies from 300 m to 700 m.

Similar to Mt. Simon, Eau Claire is absent in the south and southwest (see Figure 2b). In addition, it is absent or very thin in two areas in the west of the model domain, along the Mississippi River. Otherwise, Eau Claire is relatively thick, more than 90 m throughout most of the model domain. The continuous presence of Eau Claire, both in the core injection area and the updip areas farther north, will help to safely contain large amounts of CO_2 injected in the deep, extensive, and thick Mt. Simon Sandstone.

Mt. Simon exhibits varying rock properties in the vertical direction, caused by changes in the depositional environment. From the geophysical logs in boreholes penetrating this formation (MGSC 2005, p. 274), Mt. Simon can be divided into four major units with similar hydrogeologic properties: (1) an upper unit of sandstone and shale that was tidally influenced and deposited, (2) a thick middle unit of relatively clean sandstone, (3) an arkosic sandstone unit (rich in feldspar) of high permeability and porosity, and (4) a lower unit of moderate permeability and porosity (present only in the thickest portions of Mt. Simon). Figures 2c and 2d show the thickness of the upper and the arkosic units of Mt. Simon, as well as the location of deep boreholes used to interpolate the unit's thickness.

2.2. Spatial Variability of Rock Properties

The large number of data sets on rock porosity and permeability available for Mt. Simon show significant spatial variability at both the core and the regional scales (ISWS and Hittman Associates 1973; Buschbach and Bond 1974; Becker et al. 1978; Visocky et al. 1985; Nicholas et al. 1987; Young 1992b; MGSC 2005; O'Connor and Rush 2005; Leetaru et al. 2008). Detailed porosity logs exist for a number of vertical or subvertical wells within or near the core injection area. Among these wells is the Weaber-Horn #1 well (see Figure 2c for its location), with sonic porosity measured every 0.15 m from an elevation of -966 to -2621 m. Based on the porosity log (Figure 3), the four-unit Mt. Simon stratigraphy was further divided into 24 hydrogeologic layers, each of which has a layer-averaged porosity and permeability value (Leetaru et al. 2008). The layer-averaged values still show considerable variability, with porosity ranging from 0.062 to 0.20 and permeability from 1 to 1,000 mD. (1 mD equals 1.0×10^{-15} m^2.) As shown in Figure 3, the arkosic unit has the highest porosity and permeability, making it a good target zone for injecting CO_2. The upper unit exhibits the most significant variability in both the 0.15 m interval and layer-averaged values. The top, weathered portion of the Precambrian granite has a porosity of 0.05.

The regional-scale variability in rock porosity and permeability in Mt. Simon, analyzed using data from natural gas storage fields and large-scale aquifer tests, exhibits a trend of decreasing porosity and permeability from north to south (i.e., from shallower to deeper portions of the formation), possible because of overburden and consolidation (Birkholzer et al. 2008). The depth-averaged porosity and permeability values vary from 0.18 and several hundred mD in northern Illinois to less than 0.10 and several tens of mD in central Illinois. No well data are available for the very deep portions of Mt. Simon in southern Illinois and southern Indiana. This trend can be extended further north into southern Wisconsin, where a number of hydrogeologic investigations have been conducted because of the importance of Mt. Simon as a groundwater resource (e.g., Feinstein et al. 2005). In southern Wisconsin, the permeability of Mt. Simon is as high as a few thousand mD, based on pumping tests (Foley et al. 1953).

Because geomechanical measurements of pore compressibility on rock cores are not available for Mt. Simon, we back-calculated pore compressibility from analyses of pumping tests conducted in central Illinois and southeastern Wisconsin (Foley et al. 1953; ISWS and Hittman Associates 1973; Visocky et al. 1985). The calculated pore compressibility (β_p) of the Mt. Simon Sandstone is 3.71×10^{-10} Pa^{-1} in deeper areas of central Illinois and 6.0×10^{-10} Pa^{-1} in shallower areas of southeastern Wisconsin (Birkholzer et al. 2008). These calculated values of large-scale pore compressibility are within the range of pore compressibility reported for well-consolidated sandstones (Yale et al. 1993, Figure 3) at *in situ* effective stresses representative of Mt. Simon.

For Eau Claire, permeability values were measured at the core scale and estimated on the regional scale. A few core-scale permeability measurements conducted in the 1960s range from 3.1 to 9.2×10^{-20} m^2 (Witherspoon et al. 1962; Witherspoon and Neuman 1967; Thomas 1967). In contrast, the regional-scale vertical permeability used for the Midwest RASA (Regional Aquifer System Analysis of the United States) study ranges from 1.5×10^{-16} to 2.4×10^{-17} m^2 (Mandle and Kontis 1992). Similar differences between the core-scale permeability (1.8×10^{-21} to 4.1×10^{-19} m^2) and regional-scale vertical permeability (1.8×10^{-18} m^2) have been reported for the overlying regional aquitard of the Maquoketa Shale (Hart et al. 2006; Eaton et al. 2007).

2.3. *In Situ* Temperature and Salinity Profiles

Many temperature measurements have been recorded at the bottom of deep wells in the Illinois Basin and an isothermal map at 150 m depth was used by Cartwright (1970) to analyze temperature anomalies. For Mt. Simon, water-temperature measurements are available at several wells, varying from about 10^{o}C in the shallow portions near Chicago and southeastern Wisconsin to 24–27 ^{o}C in deeper portions farther downdip in southern Illinois (ISWS and Hittman Associates 1973, p. 13). The vertical profile of temperature observed in the USGS test well in northern Illinois (Visocky et al. 1985; Nicholas et al. 1987) was used to calculate the average temperature gradient in Mt. Simon. The calculated value is 9.2 ^{o}C/1 km depth, and is believed to represent the *in situ* conditions in most parts of the model domain

Salinity was measured in different wells at varying depths in Mt. Simon (Visocky et al. 1985; Nicholas et al. 1987). Salinity increases significantly from 235 mg/L at a depth between 299 and 454 m, to 263,000 mg/L at a depth of 2576 m. The salinity data indicate a strong linear correlation with depth (at a rate of 12.8 mg/L per meter) between 610 m and 2100 m below ground surface, as shown by a correlation coefficient of 0.96. Below 2100 m, the salinity of brine is constrained by the solubility of salt at prevailing pressure and temperature conditions, which results in a deviation from the linear fitting model. A polynomial fitting model (not shown) seems to produce a more reasonable salinity profile with depth and was therefore employed to assign *in situ* salinity for each numerical gridblock in the model domain as initial conditions. It is believed that the deviation from the polynomial fitting for the entire basin has a negligible impact on the change in brine salinity caused by CO_2 storage; more sensitive to salinity values are CO_2 density and viscosity in the core injection area only.

Due to the significant variations in elevation and thickness of Mt. Simon, it is believed that the dominant factor affecting *in situ* pressure is the depth of a given point of interest, together with *in situ* temperature and salinity. While the regional-scale discharge from and recharge into Mt. Simon were investigated by Gupta and Bair (1997) and others, it is believed that the GCS-induced pressure gradient is much higher than the *in situ* pressure gradient driving the regional groundwater flow. In addition, we are interested in the net change of *in situ* conditions induced by CO_2 storage, and therefore decided to neglect the dynamics of regional groundwater flow in our model. The *in situ* pressure was calculated assuming hydrostatic conditions, taking into account the significant variations in salinity and temperature. Vertical profiles of salinity (polynomial fitting) and temperature (10 ^{o}C/km) used in the modeling are subject to refinement as additional data becomes available during the first stages of the 3-year CO_2-injection test.

3. Modeling of the Plume- and Basin-Scale Processes

This section presents the generalized flow and transport processes at the plume and basin scale. A particular phenomenon of CO_2 accumulation, penetration and breakthrough in a stratified storage formation (with moderate contrasts in permeability and entry capillary pressure), is presented. To simulate the two-phase flow at the plume scale and the single-phase flow at the basin scale, we developed a three-dimensional model with a site-specific application to the Illinois Basin.

3.1. Plume- and Basin-Scale Processes of GCS

We are interested in a storage system consisting of a thick, brine-filled sandstone formation as storage formation and an overlying sealing unit as caprock. The storage formation comprises a number of laterally extensive, alternating high- and low-permeability layers, with a high-permeability layer at the bottom suitable for injection of CO_2. (Under the storage conditions in the deep storage formation, supercritical CO_2 prevails for pressure higher than 73.8 bar and temperature higher than 31.0 ^{o}C, and has liquid-like density) Outside the two-phase CO_2-brine flow region, it is unnecessary to distinguish these multiple layers, because vertical equilibration of GCS-induced pressure perturbations of the single-phase flow in the storage formation is quick. Note that the CO_2-rock interaction and fingering of denser brine containing dissolved CO_2 are not included in the plume-scale processes considered here.

3.1.1. Plume-Scale Processes

Physically, the two-phase flow of CO_2 and brine in the storage formation is controlled by the density difference between CO_2 and brine (i.e., buoyancy), the capillarity of sediments, and the pressure gradient caused by CO_2 injection. In addition, the contrasts in permeability and entry capillary pressure (between the high-permeability injection layer and its immediately overlying low-permeability layer, and other high- and low-permeability layer pairs) play a key role in shaping the CO_2 plume. Conceptually, as CO_2 is injected into the bottom layer, the plume first migrates laterally within the injection layer. Under buoyancy, CO_2 tends to migrate upward and accumulate under the relatively low-permeability layer, leading to a typical gravity-override plume (with plume thickness decreasing with the radial separation from the injection well) (Pruess and Garcia 2002; Nordbotten et al. 2005; Zhou et al. 2008). As the injection continues, both the lateral plume size and the plume thickness increase, leading to an increase in the pressure of the nonwetting phase (i.e., the CO_2-rich phase) at the layer interface. When the pressure at the interface exceeds the entry capillary pressure, CO_2 starts to penetrate into and eventually breaks through the low-permeability layer, entering an overlying high-permeability layer. This *accumulation-penetration-breakthrough phenomenon* in the stratified formation can significantly retard the upward migration of CO_2. Such retardation by an overlying layer of a relatively lower permeability and higher characteristic capillary pressure is called a “secondary seal effect.” The secondary seal effect mainly stems from (1) the effects of both the effective permeability (i.e., product of intrinsic permeability and relative permeability) barrier and the capillary barrier for the nonwetting CO_2 phase in low-permeability layers, and (2) the viscous fingering in high-permeability layers. (Note that CO_2 viscosity is usually 10 to 50 times smaller than brine viscosity.)

Hayek et al. (2009) found the accumulation-penetration-breakthrough phenomenon through an analytical solution for a one-dimensional multilayered system, and through numerical simulation of a two-dimensional domain representative of the Sleipner site. They underestimated the secondary seal effect by neglecting the capillary-barrier effect. However, capillary contrasts across layer interfaces play a key role in the onset of penetration, as shown in our discussion of the Illinois-Basin application below.

3.1.2. Basin-Scale Processes

The basin-scale processes relevant to multisite storage of large CO_2 volumes are (1) the propagation of pressure buildup (and brine migration) in the storage formation away from injection sites to the margins of a sedimentary basin, (2) the interference of pressure buildup between different injection sites, and (3) the attenuation of pressure buildup in the storage formation, caused by the basin-scale migration (leakage) of resident brine into and through the caprock. The migration of displaced brine in the single-phase flow regime in the storage formation and through the sealing units is governed by the density-dependent flow equations (Zhou et al. 2005). To characterize the pressure interference during the CO_2 injection period, we may define three characteristic stages of (1) an early stage dominated by local features (e.g., formation thickness) without pressure interference (from neighboring sites) at injection centers, (2) an intermediate stage when single-site behavior changes to multisite behavior, and (3) a final stage when the pressure buildup at a site is dominated by the composite behavior of all sites. Some analytical or semi-analytical solutions (Theis 1935; Hantush 1960; Zhou et al. 2009) can be used to approximately estimate the two time scales separating the three stages. The site-specific application and discussion are presented in the Results and Discussion section below.

3.2. Development of the Integrated Model

To simulate the plume- and basin-scale processes, we developed a three-dimensional model based on the geologic model, rock properties, and *in situ* conditions of salinity and temperature in the Illinois Basin. Model development consists of the determining model boundaries, generating a three-dimensional mesh, assigning rock properties, specifiying boundary conditions, and specifying initial pre-injection conditions. A hypothetical scenario of CO_2 injection and storage was considered, assuming large-scale deployment of GCS with multiple storage sites in the center of the Illinois Basin.

3.2.1. Determination of Model Domain

The domain of the 3D basin-scale model covers the northern and middle portions of the Illinois Basin. The model domain extends north to cover the shallow Mt. Simon in northern Illinois up to the south edge of the Wisconsin Arch. The domain extends west to the Mississippi River, and southwest to the Ozark Uplift in Missouri, where Mt. Simon becomes thin or disappears. To the south, the model domain ends at the extensive and dense faults zones there, and to the east, it covers the entire area of Indiana up to the middle of the Cincinnati Arch (see Figure 1). The model domain, which spans 570 km in the easting and 550 km in the northing directions, for a total area of 241,000 km^2, is sufficiently large to evaluate basin-scale pressure buildup and brine migration, and to assess the potential environmental impact on the valuable groundwater resources in northern Illinois. Mt. Simon continues to be present beyond the Illinois Basin, allowing brine to escape laterally into neighboring basins further north, west, and east. In the vertical direction, the model comprises Mt. Simon, Eau Claire, and the weathered portion of the Precambrian granite. The elevation of the model varies from -4850 m to 25 m msl.

3.2.2. CO_2 Injection Scenario

The core injection area hosting the multiple storage sites in our hypothetical scenario has a favorable geologic setting, with Mt. Simon sufficiently thick (300 to 730 m) and deep enough (1200 to 2700 m) for injection of supercritical CO_2. The area is in close proximity to various large CO_2 sources, is at least 32 km away from the nearest natural gas storage fields in operation, and contains no significant faults except the La Salle Anticlinal Belt. An array of 20 hypothetical individual injection sites was selected, with an average spacing of 30 km in the northing and 27 km in the easting directions. A possible future injection scenario with annual injection rates of 5 Mt CO_2 per storage site was considered, having a total annual injection rate of 100 Mt CO_2, which corresponds to one-third of the current annual emissions from large stationary CO_2 sources in the region (USDOE 2008). The injection was assumed to continue for 50 years. At each injection site, CO_2 is injected into the three hydrogeologic layers of the arkosic unit (see Figure 3).

3.2.3. Three-Dimensional Mesh Generation

A 3D unstructured mesh was designed as shown in a plan view in Figure 4. To capture the time-dependent evolution of the CO_2 plume around each injection site, we first generated a 2D submesh with a radial discretization varying from 20 m to 1000 m within a radius of 10 km of each injection center. There are 608 2D columns in the high-resolution submesh surrounding each injection center, to ensure accurate simulation of the CO_2 plume behavior. Outside of these submeshes, uniform columns of 2 km×2 km are used in the core injection area, increasing to columns of 5 km×5 km in the so-called near-field area, and 10 km×10 km in the so-called far-field area. The 2D mesh comprises a total of 20,408 vertical columns.

In the vertical direction, the detailed 24-layer subdivision of Mt. Simon (based on the Weaber-Horn #1 well) was used for the entire core injection area. Each of the 24 Mt. Simon hydrogeologic layers was further subdivided into several model layers, with the maximum thickness of a 3D gridblock set to 10 m. On average, there are 55 model layers for the 24 Mt. Simon hydrogeologic layers. This fine vertical resolution was considered necessary to capture the upward CO_2 migration affected by vertical heterogeneity in the core injection area. In addition, the model comprises three model layers for Eau Claire and one model layer for the 40 m thick Precambrian granite. The entire 3D mesh consists of 1,254,000 gridblocks and 3,725,000 connections between them.

3.2.4. Model-Relevant Rock Properties

As discussed in the site description section, the rock properties of Mt. Simon exhibit strong lateral and vertical variability. Within the core injection zone, the layer-averaged rock properties of the 24 hydrogeologic layers were used (shown in Figure 3) along with the Hinton #7 Well (see Figure 2c for its location) in a gas storage field just north of the core injection area. The detailed vertical variability was accounted for because the small-scale rock property variation can have a significant impact on the two-phase CO_2-brine flow processes. It was furthermore assumed that each hydrogeologic layer is laterally homogeneous and continuous in the core injection area. To account for the possibility of unaccounted discontinuities (local breaches, baffles) in these layers, which would cause increased upward migration of CO_2, the vertical permeability of very-low-permeability layers in Mt. Simon was arbitrarily increased by factors of 5 or 10.

A detailed representation of vertical variability is not necessary for the large-scale pressure perturbation in the single-phase brine flow region outside of the core injection area, because vertical pressure perturbations equilibrate quickly. Therefore, the near- and far-field areas of Mt. Simon were assigned by depth-averaged formation properties. Regional-scale permeability values of 1.0×10^{-13} m^2 and 5.0×10^{-13} m^2 were used for the near- and far-field areas, respectively, with porosity values of 0.12 and 0.16. Pore compressibility in the entire Mt. Simon was set to 3.71×10^{-10} Pa^{-1} (see Table 1). The vertical permeability of Eau Claire was set to 1.0×10^{-18} m^2. This value is close to the regional-scale permeability of the upper regional Maquoketa aquitard, and orders of magnitude higher than the core-scale permeability of both the Maquoketa and Eau Claire aquitards (Hart et al. 2006; Witherspoon and Neuman 1962). A lower permeability (1.0×10^{-19} m^2) was assigned to the Precambrian granite.

Few site-specific measurements have been made on capillary pressure and relative permeability. Thomas (1967), measuring the capillary pressure curves for two local rock samples of relatively low permeability, found that the Leverett scaling (Leverett, 1941) worked well in estimating entry capillary pressure based on measured permeability. The entry capillary pressure of all hydrogeologic layers was calculated, using Leverett scaling and the base entry capillary pressure value (α^{-1} = 6500 Pa) of the Frio Sandstone, with a porosity of 0.33 and a permeability of 8.37×10^{-13} m^2 (Sakurai et al. 2005; Doughty et al. 2008). The base value was calculated for the CO_2-brine fluid pair under the storage conditions by fitting the original drainage-test data obtained by mercury injection under a confining pressure of 124 bar (Sakurai et al. 2005), and by comparing the surface tensions and contact angles of CO_2-brine and mercury-brine fluid pairs (Bachu and Bennion 2008; Chalbaud et al. 2009). A high entry capillary pressure of 50 bar was used for Eau Claire, which is between the relatively low values (2.1 to 18.5 bar) of mudrock measured by Hildenbrand et al. (2004, Table 2) and the high values (50 to 112 bar) measured by Li et al. (2005, Table 2) under *in situ* conditions of pressure, salinity, and temperature.

3.2.5. Initial and Boundary Conditions

With the rock properties and *in situ* salinity, temperature, and pressure assigned to each gridblock, a simulation run was conducted to obtain distributions of pressure and salinity under equilibrium (hydrostatic) conditions. These distributions of pressure and salinity, as well as temperature, were used as the initial conditions for the system disturbed by CO_2 injection and storage. The fixed-pressure condition was specified at the open lateral boundaries of the model domain, with the prescribed values for equilibrium pressure and salinity, as well as zero CO_2 saturation. The fixed-pressure condition (i.e., zero pressure change from the equilibrium values) was demonstrated valid by Birkholzer and Zhou (2009) because the pressure changes (caused by CO_2 injection in the basin center) are rather small at the far-field boundaries. This condition allows resident brine to flow out of the model domain. The gridblocks at the top of Eau Claire also had a prescribed fixed-pressure boundary condition, allowing brine to flow upward into overlying formations. The bottom boundary underlying the Precambrian gridblocks was assumed to be impervious.

3.3. Simulation Runs of Using TOUGH2/ECO2N

The simulations were conducted on a Linux cluster of 72 processors using a high-performance parallel version of the TOUGH2-MP/ECO2N simulator (Pruess et al. 1999; Zhang et al. 2008). The model runs were computationally demanding because of the large number of gridblocks and connections (1.25 million gridblocks and 3.73 million connections) and the complex nonlinear processes involved. TOUGH2/ECO2N accounts for the complex thermodynamics of CO_2 migration in brine aquifers at supercritical conditions (Pruess 2005). For each of the gridblocks, three equations need to be solved for pressure, CO_2 saturation, and salt mass fraction. Since no heat sources and sinks are involved in the modeling, we employed the isothermal version of the simulator, although temperature-dependent density and viscosity of CO_2 and brine were considered internally in TOUGH2/ECO2N.

Different simulation cases were considered. A base simulation run (Case A) uses a regional-scale vertical permeability $k_v = 1.0 \times 10^{-18}$ m^2 for Eau Claire and a pore compressibility $\beta_p = 3.71 \times 10^{-10}$ Pa^{-1} for Mt. Simon. In the core injection area, the base run fully accounts for the vertical variability of Mt. Simon with respect to horizontal permeability (k_h), vertical permeability (k_v), and capillary entry pressure (α^{-1}) (Table 1). To better understand the behavior of plume-scale processes, we ran two additional cases, by changing some Mt. Simon rock properties in the upper and middle units while keeping the rock properties in the arkosic and lower units unchanged. In Case B, a constant α^{-1} of 0.5 bar was used in the upper and middle units to investigate the effect of permeability variability alone. In Case C, uniform values of $k_h = 2.16 \times 10^{-13}$ m^2, $k_v = 4.30 \times 10^{-14}$ m^2, and $\alpha^{-1} = 0.5$ bar were used for the upper and middle units. Cases A and C represent two end member scenarios of heterogeneity in permeability: Case A is for a perfectly stratified system (i.e., long-range lateral correlation length) overlying the arkosic unit, while Case C represents a system with random variability and no apparent correlation, so that uniform permeability can be assumed above the arkosic unit. These cases help us understand the inherent complexities of the plume-scale processes resulting from the spatial variability in rock properties.

For basin-scale phenomena, we conducted two additional simulation runs to take into account inherent variabilities, uncertainties, and the scale-dependence of some model parameters. In Case D, a vertical permeability of 10^{-20} m^2 was used for Eau Claire to investigate the natural attenuation of pressure buildup in the storage formation, by comparison to Case A. In Case E, the pore compressibility of Mt. Simon and the sealing units was increased by a factor of three from the base case to study the critical impact of this parameter on the magnitude and propagation of pressure buildup. Table 1 summarizes the hydrogeologic properties for all cases.

4. Results and Discussion

We focus our discussion on the following aspects: (1) the evolution and potential interference of individual CO_2 plumes during the 50-year injection period and the 150-year post-injection period, as well as the secondary seal effect; (2) the propagation and interference of pressure buildup induced by CO_2 injection at individual injection sites within the core injection area; and (3) the basin-scale pressure buildup and brine migration, and their potential impact on groundwater resources in north-central Illinois.

4.1. Evolution of CO_2 Plumes

Figures 5a-d show contours of CO_2 saturation along the vertical south-north cross section, as a function of time (5, 25, 50, and 200 years), at Site 10. For comparison, Figure 5a also illustrates the layered permeability structure of the formations, and the thickness of the arkosic unit (~80 m) and the entire Mt. Simon (~460 m). During the injection period, the CO_2 plume exhibits a complex spatial pattern: a laterally extensive *gravity-override subplume* in the arkosic unit coupled with a *pyramid-shaped subplume* in the overlying units. Following the shut-off of CO_2 injection, the plume slowly redistributes under gravity and capillarity. The shape and evolution of the CO_2 plume during the injection and post-injection period indicate a strong secondary seal effect:

retardation of upward CO_2 migration coupled with preferential viscous fingering in high-permeability layers.

As shown in Figure 5, the injected CO_2 initially migrates laterally away from the injection center within the high-permeability arkosic unit at the bottom of Mt. Simon, displacing resident brine laterally. Buoyancy forces lead to simultaneous upward movement of CO_2 until it encounters the immediately overlying low-permeability layer (Layer 20 of Mt. Simon), which has a vertical permeability of 5.95×10^{-14} m^2 and an entry capillary pressure of 0.15 bar. CO_2 accumulates under this layer and spreads out, producing a typical gravity-override subplume within the arkosic unit. The maximum extent of the subplume ranges from approximately 3.0 km at 5 year, to 5.0 km at 25 years, and to 5.5 km at 50 years. The structural slope updipping in the northwestern direction produces a minor asymmetry with slightly further migration in the northern direction, indicating that the injection-induced hydraulic gradient is dominant in comparison to the slope-driven buoyancy and gravitation.

Once the pressure of nonwetting phase CO_2 at the interface exceeds the entry pressure of the overlying low-permeability layer, the accumulated CO_2 penetrates into the overlying layer (Layer 20) and eventually breaks through to enter the next high-permeability layer. The onset of such penetration at a given radius (r) from the injection center can be determined through evaluation of competing forces: (1) the difference in capillary pressure on both sides of the layer interface with sharp changes in rock properties, and (2) the buoyancy driving force, i.e., the product of the density difference between CO_2 and brine and the CO_2 column height, $B_1(r, t)$, of the CO_2 subplume in the arkosic unit. Considering representative values of brine density $\rho_b = 1100$ kg/m^3 and supercritical CO_2 density $\rho_g = 900$ kg/m^3 in Mt. Simon, and accounting for the capillary pressure difference (less than the corresponding entry pressure difference of 0.11 bar) between the two layers, CO_2 would start penetrating from the arkosic unit into Layer 20 when the column height exceeds a threshold value of about 5.5 m. After the onset of CO_2 penetration, the driving force in the vertical column from CO_2 accumulation in the arkosic unit (i.e., increasing $B_1(r)$ with time) increases with continuous injection. With time, the above-described accumulation-penetration-breakthrough process repeats itself for other overlying pairs of high- and low-permeability layers of Mt. Simon, and the CO_2 plume migrates slowly upward towards the top of Mt. Simon. At the end of injection (50 years), the CO_2 plume has not yet reached Eau Claire, with the top of the plume being 30 m away from the top of Mt. Simon.

The accumulation-penetration-breakthrough mechanism produces a pyramid shape for the subplumes in the upper and middle units of Mt. Simon (see Figure 5). At any given time, the decrease in CO_2 column height with radial distance in the gravity-override subplume reduces the driving force for CO_2 to migrate upward into the less-permeable overlying layers. As a result, the entire CO_2 column height decreases with radius. With injection time, the plume grows in both lateral and vertical directions. However, the plume shape does not change significantly.

The significant retardation, as shown by the slow vertical migration of CO_2 plume at a rate of 7 m/year, is caused by (1) the capillary-barrier effect discussed above and (2) the effective-permeability-barrier effect. The latter stems from the small intrinsic, but also reduced, relative permeability in less permeable layers. As shown in Figures 5a through 5c, CO_2 saturation has a positive correlation with layer permeability and a negative correlation with entry capillary pressure. Such correlations produce a contrast in effective permeability that is even higher than that of intrinsic permeability. On the other hand, CO_2 accumulation in high-permeability layers produces preferential viscous fingering in the lateral direction. At 50 years, the lateral plume extent is the largest in Layer 11, one kilometer wider than the gravity-override subplume in the arkosic unit, because a stronger contrast in entry capillary pressure occurs between Layers 10 and 11 (see Figure 3).

Following the shut-off of CO_2 injection at 50 years, the CO_2 plume redevelops mainly under gravity and capillary forces. Buoyancy drives mobile CO_2 upward through already established CO_2 migration pathways. After 150 years of plume redistribution (see Figure 5d), the arkosic unit has a CO_2 saturation slightly higher than the residual gas saturation. CO_2 saturation is also close to residual gas saturation in the upper and middle units, except in layers of relatively high permeability, where CO_2 saturation is still elevated. In these layers, CO_2 migrates mostly in a lateral updip direction, producing an asymmetrical plume with a larger extent. The maximum lateral plume of 13.5 km width at 200 years occurs in Layer 11, with a projection in the northing from 703.5 km to 715 km. Overall, the lateral updip migration of CO_2 is slow, at an average rate of 3.3 m/year during the post-injection period. Note that the volume of CO_2 available for lateral migration in high-permeability layers is restricted as it stems from the slow accumulation-penetration-breakthrough process in the vertical direction. As a result, the mobile CO_2 in the underlying layers gradually depletes, with a growing volume of immobile CO_2. At 200 years, the plume has still not reached the base of the caprock.

Figure 6 shows all twenty individual CO_2 plumes at 50 and 200 years measured at the top of Layer 11, which is the layer showing the largest lateral plume extent within Mt. Simon. At 50 years, the (maximum) lateral extent of the plumes varies from 5.5 to 6.5 km, and the difference in plume size is mostly a result of differences in the Mt. Simon thickness. Each plume is approximately circular to slightly elliptical, indicating that the dominant driving force in the lateral direction comes from CO_2 injection. Minor differences in plume shape between individual sites can be attributed to the difference in the local structural slope. At 200 years, when the injection-induced pressure gradient has relaxed, asymmetry becomes more prominent in some plumes compared to others, consistent with differences in the local topography of Mt. Simon. Two representative sites are Site 4, with a small slope of 3.3 m/km, and Site 10, with a steeper slope of 17.3 m/km. The plume at Site 4 is essentially circular, with a plume size of 9 km by 9 km, while the plume at Site 10 is elliptical, with axis sizes of 13.5 km and 10.0 km. Individual plumes have not merged with each other during the first 200 years, and, because saturation is now close to residual, much further spreading to possible merging of plumes is not expected.

Figure 7a shows the calculated volumes of immobile and mobile CO_2 under storage conditions in Case A, as well as the total volume of pores with free-phase CO_2 present. For simplicity, immobile CO_2 is defined as being below residual saturation, and thus cannot move as a separate phase, while the mobile CO_2 is the free-phase CO_2 fraction higher than residual saturation and can migrate. The total pore volume (or the plume volume) is defined as the subsurface pore volume affected by free-phase CO_2 as long as CO_2 saturation is larger than zero, which is higher than the total CO_2 volume (i.e., sum of mobile and immobile CO_2 volumes). Both mobile and immobile CO_2 volumes increase with injection time. At 50 years, these volumes are 1.9×10^9 and 3.3×10^9 m^3, respectively, with the mobile CO_2 (mainly accumulated in high-permeability layers) accounting for 37% of the total CO_2 volume. The average density of free-phase CO_2 at 50 years is 890 kg/m^3. The subsurface pore volume affected by free-phase CO_2 is 14.3×10^9 m^3, with an average CO_2 saturation of 0.36. After injection stops, the volumetric fraction of mobile CO_2 decreases with time. At 200 years, the mobile CO_2 fractional volume is 0.13 of the total free-phase CO_2, while the subsurface pore volume affected by CO_2 is 19.1×10^9 m^3, with an average saturation of 0.27. Figure 7b shows the calculated fractional mass of injected CO_2 as dissolved, immobile, and mobile CO_2 in Case A. The mass fraction of dissolved CO_2 (relative to total CO_2 mass) is relatively stable at ~0.07 during the 50-year injection period, and gradually increases during the post-injection period to 0.10 at 200 years. The immobile fractional mass increases with time to 0.59 at 50 years, and continues to increase during the post-injection period to 0.77 at 200 years. Even though 13% of the CO_2 mass remains mobile at 200 years, the risk of CO_2 leakage through the caprock is very small, since, because of the secondary seal effect, the plume has not yet reached the top of Mt. Simon (see Figure 5d).

The assumption of a perfectly stratified Mt. Simon used in simulation Case A is based on a geologic interpretation of the upper unit at two gas storage fields (Morse and Leetaru 2005). Uncertainties occur when this assumption is used for the entire thickness of Mt Simon, since the number of wells penetrating through Mt Simon is small and the distance between them is large. To assess the associated uncertainties in hydrogeologic properties relevant to the plume-scale processes, and to interpret the behavior of the plume evolution and shape, we show, in Figures 5e through 5h, the resulting CO_2 plumes for Case B (with varying k but constant α^{-1} above the arkosic unit) and Case C (with constant depth-averaged k and α^{-1} above the arkosic unit). We also provide, in Figure 7, a comparison of the fractional CO_2 masses and pore volumes between Cases A and B.

Comparison of Cases A and B illustrates four main differences in the simulated plume behavior at 50 years: Case B features (1) a larger lateral extent of the gravity-override subplume in the arkosic unit because of a higher α^{-1} contrast at the interface, (2) less lateral spreading of the plume in the upper and middle units of Mt. Simon because vertical heterogeneity in capillary entry pressure is ignored, (3) migration and accumulation of CO_2 all the way to the top of Mt. Simon and spreading under Eau Claire, indicating less retardation of upward CO_2 migration, and (4) a higher fractional mass and volume of mobile CO_2. At 200 years, the differences in plume shape are even more pronounced, with most of the mobile CO_2 accumulating and spreading under the top of Mt. Simon in Case B. All these differences indicate that α^{-1} variability in the alternating layers in Case A enhances the retardation of upward CO_2 migration, i.e., *the secondary seals within the storage formation provide additional security for long-term CO_2 containment under the primary regional seal*. Note that we used an entry pressure value of 0.5 bar for the upper and middle units in Case B, which is higher than the 0.15 bar used in Case A for the layer immediately overlying the arkosic unit.

In Case C, which is essentially a two-layer system, retardation occurs only at the interface between the arkosic unit and the middle unit. The vertical permeability changes from 1.0×10^{-12} m^2 in the arkosic unit to 4.3×10^{-14} m^2 in the upper and middle units, while the entry capillary pressure changes from 0.04 to 0.50 bar. The similarity in plume characteristics between Cases B and C indicates that the strong changes between the arkosic unit and the upper and middle units play a critical role in shaping the CO_2 plumes, while additional layering with permeability differences may be less important. Comparison among all three cases suggests that additional vertical variability of capillarity in a stratified system is important in retarding upward CO_2 migration.

We may conclude that Mt. Simon has various favorable conditions for long-term, safe containment of a large volume of CO_2: (1) a thick arkosic unit of high permeability and porosity, providing high CO_2 injectivity at the bottom of the formation; (2) sharp changes in permeability and capillarity (across the interface between the arkosic unit and the middle unit), reshaping the CO_2 plume for a higher sweeping efficiency; (3) multiple alternating layers with permeability/capillarity contrasts in the middle and upper units, further retarding upward CO_2 migration; and (4) a thick regional seal, ensuring long-term CO_2 containment. In the simulation case considered most realistic (Case A), the injected CO_2 is contained within the thick stratified Mt. Simon Sandstone, with lateral spreading over the entire thickness and the CO_2 plume not even reaching the top of the storage formation. Note that similar plume characteristics showing strong lateral spreading within various high-permeability layers have been observed at the Sleipner site (Arts et al. 2004; Chadwick et al. 2007). At 200 years, the vast majority of the injected CO_2 is contained via residual and solubility trapping, leaving only 13% as mobile phase. Even when the upper and middle units of Mt. Simon are assumed homogeneous, the sharp changes in permeability and capillarity occurring between the arkosic and middle units favorably affect the plume shape (i.e., the secondary-seal effect), delaying upward migration of CO_2.

4.2. Propagation and Interference of Pressure Buildup in the Core injection Area

Resident brine displaced by injected CO_2 is stored in the additional pore space made available by pore expansion and brine density increases in response to pressure buildup. The pressure buildup increases in its magnitude with injection time and propagates away from the injection centers. The speed of propagation depends on the effective (horizontal) hydraulic diffusivity of Mt. Simon.

Figure 8 shows contours of pressure buildup observed at the top of Mt. Simon at 0.5, 5, 50, and 100 years. We focus on the core injection area in this section. In comparison with the rather slow development and limited lateral extent of CO_2 plumes, pressure buildup travels much faster and farther. After only 0.5 years of injection, the pressure buildup in most of the core injection area is higher than zero. Individual areas of elevated pressure surrounding each storage site have just merged and started to form a large continuous area of pressure increase. At later stages (5 and 50 years), a continuous elevated-pressure region develops because of pressure interference in the core injection area, even though individual pressure-buildup peaks associated with the different injection centers can be identified. After 50 years, the pressure buildup in the core injection area varies from 25 to 35 bar, with an average value of 32.9 bar and slightly higher peak values at injection centers. Pressure decreases strongly as CO_2 injection ceases, to values around 12 bar at

100 years. Pressure buildup outside of the core injection area remains essentially zero during early injection stages (0.5 and 5 years), while some far-field pressurization can be seen at 50 and 100 years (to be discussed next).

Figures 9a and b show the simulated transient pressure buildup and its time derivative at eight observation points (see Figure 2a for their locations) along the south-north cross section. Observation Points 1, 3, and 5 correspond to injection centers, Points 2 and 4 are in the core injection area between injection centers, and Points 6, 7, and 8 are outside of the core injection area at increasing distance from the center of the core injection area. Figure 9c shows the simulated pressure buildup at all 20 injection centers, at different times (0.5, 5, 10, 30, and 50 years), while Figure 9d explores the correlation between pressure buildup and the Mt. Simon thickness at injection centers at 0.5, 5, and 50 years.

Three stages (the early, intermediate, and final stages) of pressure-buildup propagation and interference can be identified in the pressure buildup plots in Figures 9a and 9b. During the early stage (up to $t_{ei} \approx 0.5$ year), the increase in pressure at each injection site is largely independent of the other sites. This is evident from very small pressure buildup at Observation Points 2 and 4, situated in between of injection centers (Figure 9a). The magnitude of pressure buildup at injection centers depends mostly on the thickness of Mt. Simon, because the CO_2 mass injection rate is the same for all the sites, the effective hydraulic diffusivity is the same, and the variability of CO_2 density in the core injection area is relatively small. This assessment is supported by the good correlation between pressurization and thickness (with a correlation coefficient of 0.89) at 0.5 years, shown in Figure 9d, and the consistency of pressure buildup between Sites 8, 9, and 10 during the early stage in Figure 9a.

During the intermediate stage ($0.5 \leq t \leq 5$ years), the pressure buildup at each injection site is clearly affected by pressure interference from neighboring sites. Pressure has started to increase at Observation Points 2 and 4, while the rate of pressure buildup with log(t) at injection centers (Observation Points 1, 3, and 5) has started to increase (Figures 9a and 9b). Meanwhile, because of pressure superposition, the magnitude of pressure buildup at each site becomes more correlated with the number of neighboring sites (Figure 9c), while local storage-formation thickness become less relevant (see Figure 9d).

During the final stage ($5 \leq t \leq 50$ years), pressure buildup at any point within the core injection area (i.e., Observation Points 1 through 5) continues to increase at a quasi-steady rate with $\log(t)$. At 50 years, the pressure buildup is mostly driven by the composite behavior of all injection sites in the area; the correlation between pressurization and thickness completely disappears (see Figure 9d). In other words, the maximum pressure buildup expected at each site is only marginally affected by local features, although the overall variation of the storage-formation thickness over a larger scale does have an impact on the propagation and interference of pressure buildup.

We can assess whether the simulated pressure buildup may affect the geomechanical integrity of the Eau Claire caprock by comparing the fractional pressure buildup (relative to the pre-injection *in situ* pressure) and the regulated value. The pre-injection pressure under the assumed hydrostatic condition at the 20 injection centers varies significantly, from 136.0 bar at Site 1 to 279.3 bar at Site 13 (values given at the top of Mt. Simon). At the end of the injection period, the fractional pressure buildup varies from 0.12 at Site 13 to 0.22 at Site 2, with an average value of 0.18. This value is slightly higher than the value of 0.13 (corresponding to an injection pressure gradient of 12.44 kPa/m, with an assumed brine density of 1100 kg/m^3) commonly used for natural gas storage fields in Illinois and Indiana. However, the simulated fractional pressure buildup is less than the regulated value of 0.65 (corresponding to the regulated injection pressure gradient of 18.1 kPa/m) in Illinois and Indiana, and far less than 1.05, which corresponds to a fracturing gradient of 22.6 kPa/m used by fracture stimulation companies in the Illinois Basin (USEPA 1994; MGSC 2005, p312). This indicates that the expected pressure buildup in the simulated GCS scenario should not cause damage to the caprock in the core injection area.

4.3. Basin-Scale Processes and Potential Environmental Impacts

Pressure buildup and brine migration are not confined to the core injection area. As shown in Figures 8c and 8d, pressure changes propagate away from the central core injection area to the margins of the deep sedimentary basin, driven by the combined effect of CO_2 injection at the 20 injection sites.

4.3.1. Basin-Scale Pressure Buildup

Figure 8c shows the simulated pressure buildup in the model domain at the end of the 50-year injection period. Elevated pressure occurs in Mt. Simon over the entire basin, affecting a pore volume of 11.2×10^{12} m^3 and an area of 241,000 km^2. The pressure-affected pore volume is orders of magnitude larger than the subsurface pore volume affected by free-phase CO_2 (14.3×10^9 m^3). The pressure buildup at 50 years is about 10 bar at the margin of the core injection area, about 1 bar at the margin of the near-field area, and about 0.1 bar at the basin margin. Moderate pressure perturbation of up to 1 bar occurs in northern Illinois, where groundwater resources overlying Eau Claire are important for water supply. Following the shut-off of CO_2 injection, the pressure decreases in the core injection area, but continues to increase in the far-field area (see Figure 8d). At 100 years, the pressure buildup close to the northern model boundary is 0.2 bar, where a boundary condition of zero pressure change limits further increase, and brine is allowed to leave the model domain into neighboring basins. With time, the system would continue to slowly progress towards a new quasi-equilibrated state, with pressure eventually returning to hydrostatic conditions, long after CO_2 injection stops.

4.3.2. Basin-Scale Brine Migration

Brine migration processes are evaluated here through analysis of the volumetric balance of resident brine displaced by injected CO_2 and through evaluation of salinity changes caused by brine transport. Figure 10a shows the volumetric balance of displaced brine as a function of time. Displaced brine (1) occupies the additional pore space made available by brine and pore compressibilities in response to pressure buildup, (2) migrates through the top of Eau Claire into overlying formations, and (3) flows out of the system into neighboring basins through lateral open boundaries. At each time, the volume of displaced brine is identical to the volume of free-phase CO_2 under storage pressure and temperature conditions. The volume of dissolved CO_2 is negligible because the specific volume of dissolved CO_2 in resident brine is very small (Pruess and Garcia 2002). Figure 10b further elaborates on the characteristics of brine leakage through the caprock, showing leakage rates separately for the core injection area and the near- and far-field areas, as well as for the total leakage rate.

We calculated (a) the time (t_{cp}) needed for full penetration of a pressure perturbation through Eau Claire, and (b) the time (t_{ss}) needed to reach steady-state conditions in the caprock (a linear pressure profile). These calculations are $t_{cp} = 0.05B_s^2 / D_{vs}$ and $t_{ss} = 0.45B_s^2 / D_{vs}$ (Crank 1975, p. 50-51), where B_s and D_{vs} $(= k_{vs} / \phi\mu_b(\beta_b + \beta_{sp}))$ are the thickness and hydraulic diffusivity of the caprock. The hydraulic diffusivity, calculated using seal vertical permeability k_{vs} = 10^{-18} m^2, seal porosity ϕ_s = 0.15, brine viscosity $\mu_b = 0.5 \times 10^{-3}$ Pa.s, brine compressibility $\beta_b = 3.4\times 10^{-10}$ Pa^{-1} (the fluid properties representative of a deep saline aquifer), and seal pore compressibility β_{ps} = 7.4×0^{-10} Pa^{-1}, is $D_{vs} = 1.23 \times 10^{-5}$ m^2/s. It would take about 2 years for a pressure perturbation to penetrate through Eau Claire and about 12 years to arrive at a linear pressure profile within this formation. Thus, we should expect brine leakage to be very small during the early injection years. Indeed, during the first 5 years, the displaced brine is almost completely accommodated by the pressure-induced (available) pore volume increase, with negligible volumes of leaked brine and out-flowing brine. Thereafter, brine leakage starts to become relevant. At 50 years, the total leakage rate is 22.7×10^6 m^3/year, accounting for 22% of the total brine displacement rate (103.3×10^6 m^3/year). The cumulative volume of brine leakage (0.49×10^9 m^3) represents 9.5% of the total volume of displaced brine (5.16×10^9 m^3). In contrast, brine flow through open lateral boundaries remains small during the first 50 years. During the injection period, the majority of the displaced brine (90%) is stored in the system through (available) pore volume increases induced by pressure buildup and brine and pore compressibility.

After CO_2 injection ceases, the volume of displaced brine slightly decreases with time, a net result of two counteracting effects. The first is the increase in dissolved CO_2 mass, whose specific volume in brine is negligible, and the second is the expanding free-phase CO_2 volume caused by pressure reduction. As overall pressure decreases and the system slowly evolves to pressure re-equilibration, more and more brine leaves the model domain both upward into overlying formations and laterally into neighboring basins. At 200 years, the cumulative volumes of brine outflow and leakage are 0.9×10^9 m^3 and 3.1×10^9 m^3, respectively, accounting for 18% and 62% of the total volume of displaced brine (5.1×10^9 m^3) (Figure 10a). This leaves only 20% of the displaced brine volume in the additional pore volume of the system in response to residual pressure buildup. The total leakage rate reaches its maximum value of 26.1×10^6 m^3/year at 63 years, after which it gradually decreases (Figure 10b). Whether these transport processes constitute environmental concerns for groundwater resources is further discussed in the next section.

The basin-scale brine migration induces salinity changes within the model domain. However, these changes are very small in the near- and far-field areas. After 50 years, the maximum salinity change of ~0.2% relative to pre-injection conditions occurs in the single-phase flow region just outside of CO_2 plumes. The simulated salinity changes are essentially zero farther away from the CO_2 plumes, in the core injection area as well as in the near- and far-field areas. These negligible effects are consistent with the small travel distance of particles for the time scale of interest (i.e., hundreds of years or so). In other words, while overall large volumes of brine are being displaced, the injection-induced flow velocities are small, and thus lateral migration distances are minor in the near- and far-field areas. We conclude that changes in salinity within Mt. Simon are not a direct concern to groundwater quality in northern Illinois.

4.3.3. Potential Environmental Impacts

The impact of large-scale pressure buildup in Mt. Simon on groundwater resources cannot be directly assessed in this study, because the overlying freshwater aquifers (the Ironton-Galesville Aquifer and the St. Peter Aquifer) in northern and central Illinois and the freshwater portion of the Mt. Simon aquifer further updip in southern Wisconsin are not included in our model. However, we may discuss potential environmental implications based on the simulated basin-scale pressure buildup and brine migration results presented above. Note that in most of the model domain, the current (pre-injection) hydraulic gradients result in upward groundwater flow from Mt. Simon to the overlying aquifers, except in the central-northern Illinois, where the Maquoketa aquitard is absent and recharge into Mt Simon occurs (Mandle and Kontis 1992). The GCS-induced hydraulic gradients through Eau Claire will enhance groundwater discharge from Mt. Simon in most of the model domain, in particular in the core injection area.

The direct hydrological and hydrochemical impact on the updip Mt. Simon aquifer in southern Wisconsin can be considered insignificant. Whereas groundwater pumping from Mt. Simon in northern Illinois was terminated in the 1970s because of pumping-induced salinity increases (Burch 2002, p. 11), the GCS-induced salinity changes as observed in our model results are essentially zero, due to the very small migration distance in northern Illinois. Thus, salinity impacts in southern Wisconsin, far away from the core injection zone, should be negligible. Furthermore, the magnitude of pressure buildup is less than 0.1 bar or 1 m of water head close to the northern model boundary, and should be even less further north in Wisconsin. Such increases in hydraulic head are smaller than the seasonal variations in the confined Mt. Simon aquifer caused by local recharge and discharge, and are within the regional groundwater prediction uncertainties.

In northern and central Illinois, however, CO_2 storage and resulting brine migration might affect the overlying Ironton-Galesville and St. Peter freshwater aquifers, situated under the regional Maquoketa aquitard (Young 1992a, b; Mandle and Kontis 1992). To provide a perspective, we compare the GCS-induced pressure buildup in the core injection area of deep Mt. Simon to the pumping-induced drawdown in shallower Mt. Simon in the eight-county metro-Chicago region (this area visualized in grey shading in Figure 8a). The groundwater pumping in northern Illinois occurs mainly from the Ironton-Galesville and St. Peter aquifers. Figure 11a shows the historic pumping rate in this region and the total pumping rate in northern and central Illinois. The pumping rate steadily increases from 1860 to the 1980s, and then declines after groundwater was supplemented by freshwater from Lake Michigan. During the 50 years from 1940 to 1990, the average annual pumping rate in the metro-Chicago region is 169.4×10^6 m^3/year, about 70% higher than the assumed volumetric rate of CO_2 storage in our modeling scenario. As a result, a significant drawdown of 25 bar occurred in these freshwater aquifers and the Mt Simon aquifer in the 1980s and early 1990s (Mandle and Kontis 1992; Visocky 1997; Burch 2002). As shown in Figure 11b, the total effect of pumping-induced drawdown is comparable in magnitude to that of pressure buildup after 50 years of CO_2 injection shown in Figure 8c. In addition to the metro-Chicago region, groundwater pumping occurs in the other counties in central and northern Illinois (see Figure 8a for their locations), accounting for about 40% of the total pumping rate in north-central Illinois.

The impact of the GCS-induced pressure buildup in Mt Simon on the overlying freshwater aquifers can be understood in two ways. First, the pressure-driven brine leakage is relatively small in northern Illinois in the simulated CO_2 injection and storage scenario. The predicted pressure changes in the northern portions of Mt. Simon (where overlying aquifers are heavily pumped) range 0.1–0.5 bar at 50 years of injection to 0.2–1.0 bar at 100 years, which provides a driving force pushing resident brine upward. During the 200-year simulation period, the cumulative volume of brine leakage from Mt. Simon into overlying aquifers is 0.36×10^9 m^3, accounting for 7% of the total volume of displaced brine. As shown in Figure 10b, most of this leakage occurs in the core injection and near-field areas, while the far-field area is less significant. The total leakage rate in the far-field area shows a maximum value of 2.7×10^6 m^3/year at 125 years, which corresponds to 17 m^3/year per square kilometer (or 0.02 mm/year). Secondly, pressure-driven brine leakage through caprock imperfections (such as leaky faults, unplugged wells) may locally increase the salinity of overlying freshwater aquifers. Evaluation of such localized effects needs further research. However, the pumping-induced drawdown has created pressure gradients between Mt. Simon and the overlying freshwater aquifers that are larger than those related to the simulated GCS scenario. If these conditions do not generate local water quality issues related to upward migration of brine, then the rather moderate gradients induced by GCS are unlikely to be problematic.

Compared to the small fractional leakage (of displaced brine volume) in the far-field area, brine leakage in the core injection area is more significant. The cumulated leakage volume for 200 years is 1.57×10^9 m^3, which accounts for 31% of the total volume of displaced brine. The maximum leakage rate is 15.6×10^6 m^3/year (see Figure 10b), which corresponds to 650 m^3/year per square kilometer (or 0.65 mm/year). As mentioned above, localized caprock imperfections may have some adverse impact on the water quality of overlying freshwater aquifers, though groundwater pumped from bedrock aquifers in this area is very small. Also, this portion of Mt. Simon is much deeper than the areas in northern Illinois, and the immediately overlying aquifers are saline as well. Evidence of brine intrusion and groundwater discharge into shallow aquifers through leaky faults under *in situ* conditions were reported by Cartwright (1970), using temperature and salinity anomalies at a depth of 150 m. However, no direct evidence of leakage for the deeper Mt. Simon-Eau Claire system is available.

4.4. Further Sensitivity Analyses on Basin-Scale Properties

Two additional sensitivity studies were conducted by varying (1) caprock permeability in Case D and (2) pore compressibility in Case E (see Table 1). While the CO_2 plume characteristics are not affected by these large-scale properties, the simulation results in these cases show different pressure buildup, as well as brine migration and leakage, at the basin scale, when compared to the base case (Case A). As shown in Figure 8e, the pressure buildup over the entire model domain is higher in Case D than in Case A, because brine leakage is negligible. In Case D, a very low-permeability seal (1.0×10^{-20} m^2) is assumed representing undisturbed shale. A pressure change in the storage formation would take approximately 130 years to penetrate Eau Claire. In contrast, Case A uses a larger seal permeability, representing the effective basin-scale permeability of a caprock with some local imperfections. As shown by the difference in brine leakage rate and volume, the caprock permeability plays a critical role in attenuating pressure buildup in Mt. Simon.

In comparison to Case A, the pressure buildup in Case E is reduced in both magnitude and lateral extent, because the higher pore compressibility allows for more storativity in response to a given pressure increase. The simulated pressure buildup in the core injection area is 10 bar less in Case E than in Case A, demonstrating strong sensitivity with respect to pore compressibility. We believe that the pore compressibility used in the base case is reasonable, and the corresponding simulated pressure buildup is representative. This is because a large number of pumping tests conducted in Mt. Simon in central Illinois and southeastern Wisconsin show pore compressibility ranging between 3.7 and 6.0×10^{-10} Pa^{-1}.

5. Summary and Conclusions

To better understand the large-scale impact of geologic carbon sequestration in a full-scale deployment scenario, we developed a three-dimensional two-phase reservoir model for the Illinois sedimentary basin. The model covers a total area of 241,000 km^2, including a core injection area of 24,000 km^2 that hosts 20 hypothetical injection sites, and near- and far-field areas where environmental impact needs to be assessed. Vertically, the model consists of Precambrian bedrock, the Mt. Simon Sandstone as the storage formation, and the overlying Eau Claire Shale as a regional seal. The model honors the detailed data of geologic settings, rock properties, ambient temperature, and salinity conditions, over the entire lateral model domain and over an extensive depth range of up to 5000 m. An unstructured 3D mesh with over one million gridblocks was generated, with local refinement around each injection site. A storage scenario was assumed, with an injection rate of 5 Mt CO_2/year over 50 years for each of the injection sites, which are spaced approximately 30 km apart. This corresponds to one third of the current annual CO_2 emissions from stationary sources in the region. The model integrates large-scale processes, such as basin-scale pressure buildup and brine migration, with plume-scale processes in the stratified storage formation.

The simulated CO_2 plume behavior indicates favorable conditions for safe storage of large volumes of CO_2 in the Mt. Simon aquifer in the Illinois Basin. These conditions include (1) a thick unit of high porosity and permeability, ensuring high injectivity at the bottom of Mt. Simon, (2) extensive alternating layers of shaley and sandy deposits in the middle and upper units of Mt. Simon, providing significant retardation of upward CO_2 migration, and (3) the thick, low-permeability Eau Claire Formation for structural trapping of CO_2. The overall shape of the CO_2 plume at each site (consisting of a gravity-override subplume in the deeper injection unit and an overlying pyramid-shaped subplume) in the storage formation is attributed to the secondary seal effect. This effect is caused by an intra-storage-formation layer (secondary seal) of relatively low-permeability and high-entry capillary pressure, and stems from the coupling of retarded CO_2 upward migration with preferential lateral CO_2 viscous fingering along high-permeability layers. This effect is observed during the injection period and during the post-injection period, when most CO_2 plumes migrate slowly along updipping layers to the north. No interference of CO_2 plumes is observed during the 200-year simulation period, and is expected at later stages because CO_2 becomes essentially immobile as a result of solubility and residual trapping.

Unlike the CO_2 plumes, the pressure buildup in response to CO_2 injection travels fast and far. In the core injection area in the center of the basin, the pressure behavior shows three characteristic stages: an early stage without pressure interference at injection centers, an intermediate stage of transient pressure interference between individual injection sites, and a final stage where a continuous pressure buildup is driven by the composite behavior of all injection sites. At 50 years of injection, the simulated pressure buildup ranges from 25 to 35 bar within the core injection area. This corresponds to a fractional pressure buildup of 0.12 to 0.22, smaller than the regulated value of 0.65 and thus ensuring the integrity of the Eau Claire caprock. From a geomechanical standpoint, 100 Mt CO_2 per year or more can be safely injected into the Mt. Simon Sandstone over an extended period of time. Pressure perturbations propagate from the core injection area all the way to the margins of the model domain, affecting a subsurface pore volume of $11{,}150 \times 10^9$ m^3, which is significantly larger than the pore volume of CO_2 plumes of 14×10^9 m^3 at 50 years. A pressure change of 1 bar and 0.1 bar can be expected as far as 150 and 300 km from the core injection area, respectively. The pressure-affected areas include regions in northern Illinois, where significant amounts of groundwater have been pumped from overlying freshwater aquifers.

As our simulation results show, the pressure buildup in Mt. Simon has the capability of pushing brine upward through the Eau Claire caprock into overlying formations. We have calculated brine leakage with a basin-scale permeability representative of local caprock imperfections (e.g., leaky faults, unplugged wells, higher sand content). The fractional leakage rate (relative to the volumetric rate of brine displaced by stored CO_2) increases from 0.0 to 0.22 at 50 years, and the cumulative volume of leaked brine accounts for 9.5% of the total volume of displaced brine at 50 years, and 62% at 200 years. Most of this leakage occurs in the core injection area in deeper parts of Mt. Simon, where directly overlying aquifers are saline and shallow freshwater aquifers are not heavily utilized. A smaller fraction of total brine leakage occurs in northern Illinois; however, it is believed that the possible localized brine intrusion, induced by CO_2 injection and storage, into the overlying freshwater aquifers is less significant than that caused by the historic and continuous groundwater pumping in northern and central Illinois. Updip brine migration within Mt. Simon to the north is essentially zero outside of the core injection area, thus posing no threat to the freshwater portion of Mt. Simon in southern Wisconsin.

Acknowledgment

The authors wish to thank Hannes Leetaru, Scott Frailey, Robert Finley, David G. Morse, and other colleagues at the Illinois State Geological Survey. Thanks are also due to John McCray and three anonymous reviewers for their constructive suggestions for improving the quality of the manuscript, and to Stefan Finsterle of Lawrence Berkeley National Laboratory for internal review. This work was funded by the Assistant Secretary for Fossil Energy, Office of Sequestration, Hydrogen, and Clean Coal Fuels, National Energy Technology Laboratory (NETL), of the U.S. Department of Energy under Contract No. DE-AC02-05CH11231. The project is jointly coordinated by NETL and the U.S. Environmental Protection Agency.

References

Arts, R., O. Eiken, A. Chadwick, P. Zweigel, L. Van der Meer, and B. Zinszner. 2004. Monitoring of CO_2 injected at Sleipner using time-lapse seismic data. *Energy* 29, no. 9-10: 1383–1392.

Bachu, S., and B. Bennion, 2008. Effects of in-situ conditions on relative permeability characteristics of CO_2-brine systems. Environmental Geology 54, no. 8: 1707–1722.

Bachu, S., W.D. Gunter, and E.H. Perkins. 1994. Aquifer disposal of CO_2: Hydrodynamic and mineral trapping. *Energy Conversion and Management* 35, no. 4: 269–279.

Becker, L.E., A.J. Hreha, and T.A. Dawson. 1978. Pre-Knox (Cambrian) stratigraphy in Indiana. Bulletin 57, Indiana State Geological Survey, Department of Natural Resources, Indiana, USA.

Bickle M., A. Chadwick, H.E. Huppert, M. Hallworth, and S. Lyle. 2007. Modelling carbon dioxide accumulation at Sleipner: Implications for underground carbon storage. *Earth and Planetary Science Letters* 255, no. 1-2: 164–176.

Birkholzer, J.T., and Q. Zhou. 2009. Basin-scale hydrogeological impacts of CO_2 storage: Regulatory and capacity implications. *International Journal of Greenhouse Gas Control* 3, no. 6: doi:10.1016/j.ijggc.2009.07.002.

Birkholzer, J.T., Q. Zhou, K. Zhang, P. Jordan, J. Rutqvist, and C.F. Tsang. 2008. Research project on CO_2 geological storage and groundwater resources: Large-scale hydrogeological evaluation and impact on groundwater systems, annual report, October 1, 2007 to September 30, 2008. Lawrence Berkeley National Laboratory, Berkeley, CA, USA.

Birkholzer, J.T., Q. Zhou, and C.F. Tsang. 2009. Large-scale impact of CO_2 storage in deep saline aquifers: A sensitivity study on pressure response in stratified systems. *International Journal of Greenhouse Gas Control* 3, no. 2: 181-194.

Burch, S.L. 2002. A comparison of potentiometric surfaces for the Cambrian-Ordovician aquifers of northeastern Illinois, 1995 and 2000. Data/Case Study 2002-02, Illinois State Water Survey, Champaign, Illinois, USA.

Buschbach, T.C., and D.R. Kolata. 1991. Regional setting of the Illinois Basin. In *Interior Cratonic Basins*, ed. by M.W. Leighton, D.R. Kolata, D.F. Oltz, and J.J. Eidel, 29–55. Memoir 51 of American Association of Petroleum Geologists, Tulsa, Oklahoma.

Buschbach, T.C., and D.C. Bond. 1974. Underground storage of natural gas in Illinois–1973. Illinois Petroleum 101, Illinois State Geological Survey, Champaign, Illinois, USA.

Cartwright, K. 1970. Groundwater discharge in the Illinois Basin as suggested by temperature anomalies. *Water Resources Research* 6, no. 3: 912-918.

Chadwick, A., R. Arts, C. Bernstone, F. May, S. Thibeau, and P. Zweigel. 2007. Best practice for the storage of CO_2 in saline aquifers: Observations and guidelines from the SACS and CO2STORE projects.

Chalbaud, C., M. Robin, J.M. Lombard, F. Martin, P. Egermann, and H. Bertin, 2009. Interfacial tension measurements and wettability evaluation for geological CO_2 storage. *Advances in Water Resources* 32, no. 1: 98–109.

Crank, J. 1975. *The Mathematics of Diffusion*, 2nd ed. Oxford University Press, Oxford, United Kingdom.

Daley, T.M., L.R. Myer, J.E. Peterson, E.L. Majer, and G.M. Hoversten. 2008. Time-lapse crosswell seismic and VSP monitoring of injected CO_2 in a brine aquifer. *Environmental Geology* 54, no. 8: 1657-1665.

Doughty, C., B.M. Freifeld, and R.C. Trautz. 2008. Site characterization for CO_2

geologic storage and vice versa: The Frio brine pilot, Texas, USA as a case study. *Environmental Geology* 54, no. 8: 1635-1656.

Eaton T.T., M.P. Anderson, and K.R. Bradbury. 2007. Fracture control of ground water flow and water chemistry in a rock aquitard. *Ground Water* 45, no. 5: 601-615.

Feinstein D.T., T.T. Eaton, D.J. Hart, J.T. Krohelski, and K.R. Bradbury. 2005. A regional aquifer model for southeastern Wisconsin. Technical Report 41, the Southeastern Wisconsin Regional Planning Commission, Madison, Wisconsin, USA.

Foley, F.C., W.C. Walton, and W.J. Drescher. 1953. Ground-water conditions in the Milwaukee-Waukesha area, Wisconsin. Water-Supply Paper 1229, U.S. Geological Survey, Washington, DC, USA.

Freifeld, B.M., R.C. Trautz, Y.K. Kharaka, T.J. Phelps, L.R. Myer, S.D. Hovorka, and D.J. Collins. 2005. The U-tube: a novel system for acquiring borehole fluid samples from a deep geologic CO_2 sequestration experiment. *Journal of Geophysical Research* 110, B10203, doi:10.1029/2005JB003735.

Gupta, N., and E. Bair. 1997. Variable-density flow in the midcontinent basins and arches region of the United States. *Water Resources Research* 33, no. 8: 1785-1802.

Hantush, M.S. 1960. Modification of the theory of leaky aquifers. *Journal of Geophysical Research* 65, no. 11: 3713-3725

Hart, D.J., K.R. Bradbury, and D.T. Feinstein. 2006. The vertical hydraulic conductivity of an aquitard at two spatial scales. *Ground Water* 44, no. 2: 201-211.

Hayek, M., E. Mouche, and C. Mügler. 2009. Modeling vertical stratification of CO_2 injected into a deep layered aquifer. *Advances in Water Resources* 32, no. 3: 450-462.

Hildenbrand, A., S. Schlömer, B.M. Krooss, and R. Littke. 2004. Gas breakthrough experiments on politic rocks: comparative study with N_2, CO_2, and CH_4. *Geofluids* 4, no. 1: 61–80.

Hovorka, S.D., S.M. Benson, C. Doughty, B.M. Freifeld, S. Sakurai, T.M. Daley, Y.K. Kharaka, M.H. Holtz, R.C. Trautz, H.S. Nance, L.R. Meyer, and K.G. Knauss. 2006. Measuring permanence of CO_2 storage in saline formations: The Frio experiment. *Environmental Geosciences* 13, no. 2: 105-121

IPCC (Intergovernmental Panel on Climate Change), 2005. *IPCC Special Report on Carbon Dioxide Capture and Storage*. Cambridge University Press, New York.

ISWS (Illinois State Water Survey) and Hittman Associates. 1973. Feasibility study on desalting brackish water from the Mt. Simon aquifer in northeastern Illinois. Urbana, Illinois, USA.

Leetaru, H.E., S.M. Frailey, J. Damico, R. Finley, J.H. McBride, and D.G. Morse. 2008. Developing a geological model for the phase III (ADM) saline sequestration validation site. Proceedings of the 7th Annual Conference on Carbon Capture and Sequestration, May 2008, Pittsburgh, PA.

Leverett, M.C. 1941. Capillary behaviour in porous solids. *Transactions of the AIME* 142, 159–172.

Li, S., M. Dong, Z. Li, S. Huang, H. Qing, and E. Nickel. 2005. Gas breakthrough pressure for hydrocarbon reservoir seal rocks: Implications for the security of long-term CO_2 storage in the Weyburn field. *Geofluids* 5, no. 4: 326-334.

Mandle, R.J., and A.L. Kontis. 1992. Simulation of regional ground-water flow in the Cambrian-Ordovician aquifer system in the northern Midwest, United States. Professional Paper 1405-C, U.S. Geological Survey, USA.

MGSC (Midwest Geological Sequestration Consortium). 2005. An assessment of geological carbon sequestration options in the Illinois Basin. Final Report, December 31, 2005, Urbana, Illinois, USA.

Morse, D.G., and H.E. Leetaru. 2005. Reservoir characterization and three-dimensional models of Mt. Simon gas storage fields in the Illinois Basin. Circular 567, Illinois State Geological Survey, Champaign, IL, USA.

Nicholas, J.R., M.G. Sherrill, and H.L. Young. 1987. Hydrogeology of the Cambrian-Ordovician Aquifer System at a test well in northeastern Illinois. Water Resources Investigations Open-File Report 84-4165, U.S. Geological Survey, USA.

Nicot, J.P. 2008. Evaluation of large-scale CO_2 storage on fresh-water sections of aquifers: An example from the Texas Gulf Coast Basin. *International Journal of Greenhouse Gas Control* 2, no. 4: 582–593.

Nordbotten, J.M., M.A. Celia, and S. Bachu, 2005. Injection and storage of CO_2 in deep saline aquifers: Analytical solutions for CO_2 plume evolution during injection. *Transport in Porous media* 58, no. 3: 339–360.

O'Connor W.K., and G.E., Rush. 2005. CO_2 flood tests on whole core samples of the Mt. Simon Sandstone, Illinois Basin. Report DOE/ARC-2005-013, Albany Research Center, U.S Department of Energy, Albany, OR, USA.

Pruess, K. 2005. ECO2N: A TOUGH2 fluid property module for mixtures of water, NaCl, and CO_2. LBNL-57952, Lawrence Berkeley National Laboratory, Berkeley, CA, USA.

Pruess, K. and J. Garcia. 2002. Multiphase flow dynamics during CO_2 disposal into saline aquifers. *Environmental Geology* 42, no. 2-3: 282–295.

Pruess, K., C. Oldenburg, and G. Moridis. 1999. TOUGH2 user's guide. Report LBNL-43134, Lawrence Berkeley National Laboratory, Berkeley, CA, USA.

Sakurai S., T.S. Ramakrishnan, A. Boyd, N. Mueller, and S.D. Hovorka. 2005. Monitoring saturation changes of CO_2 sequestration: petrophysical support of the Frio brine pilot experiment. Paper presented at Society of Petrophysicists and Well Log Analysts 46th Annual Logging Symposium, 26–29 June 2005, New Orleans, LA.

Schowalter, T.T. 1979. Mechanics of secondary hydrocarbon migration and entrapment. *The American Association of Petroleum Geologists Bulletin* 63, no. 5: 723-760.

Steinberg, M. 1992. History of CO_2 greenhouse gas mitigation technologies. *Energy Conversion and Management* 33, no. 5-8: 311-315.

Theis, C.V. 1935. The relation between the lowering of the piezometric surface head and the rate and duration of discharge of a well using ground-water storage. *Eos Transactions AGU* 16, 519-524

Thomas, L.K. 1967. Threshold pressure phenomena in porous media. Ph.D. diss., University of Michigan.

USDOE (U.S. Department of Energy). 2008. Carbon sequestration atlas of the United States and Canada, 2^{nd} Ed. National Energy Technology Laboratory, Pittsburgh, PA, USA.

USEPA (U.S. Environmental Protection Agency). 1994. Determination of maximum injection pressure for Class I wells, United States Environmental Protection Agency Region 5—Underground injection control section regional guidance #7. EPA, Washington DC, USA.

Van der Meer, L.G.H. 1992. Investigations regarding the storage of carbon dioxide in aquifers in the Netherlands. *Energy Conversion and Management* 33, no. 5–8: 611–618.

van Genuchten, M.T. 1980. A closed-form equation for predicting the hydraulic conductivity of unsaturated soils. *Soil Science Society of America Journal* 44, 892–898.

Visocky, A.P. 1997. Water-level trends and pumpage in the Deep Bedrock Aquifers in the Chicago Region, 1991-1995. Circular 182, Illinois State Water Survey, Champaign, IL, USA.

Visocky, A.P., M.G. Sherrill, and K. Cartwright. 1985. Geology, hydrology, and water quality of the Cambrian and Ordovician systems in northern Illinois. Cooperative Groundwater Report 10, State of Illinois Department of Energy and Natural Resources, Champaign, IL, USA.

Witherspoon, P., and S. Neuman. 1967. Evaluating a lightly permeable caprock in aquifer gas storage, 1: Caprock of infinite thickness. *Transactions of AIME* 240, p949.

Witherspoon, P.A., T.D. Mueller, and R.W. Donovan. 1962. Evaluation of underground gas storage conditions in aquifers through investigations of groundwater hydrology. *Journal of Petroleum Technology* 14, no. 5: 555-562.

Yale, D.P., G.W. Nabor, and J.A. Russell. 1993. Application of variable formation compressibility for improved reservoir analysis. SPE 26647.

Yamamoto, H., K. Zhang, K. Karasaki, A. Marui, H. Uehara, and N. Nishikawa, 2009. Numerical investigation concerning the impact of CO_2 geologic storage on regional groundwater flow, *International Journal of Greenhouse Gas Control* 3, no. 5: 586–599.

Young, H.L. 1992a. Summary of ground-water hydrology of the Cambrian-Ordovician aquifer system in the northern Midwest, United States. Professional Paper 1405-A, U.S. Geological Survey, USA.

Young, H.L. 1992b. Hydrogeology of the Cambrian-Ordovician aquifer system in the northern Midwest, United States. Professional Paper 1405-B, U.S. Geological Survey, USA.

Zhang, K., Y.S. Wu, and K. Pruess. 2008. User's guide for TOUGH2-MP—A massively parallel version of the TOUGH2 code. Report LBNL-315E, Lawrence Berkeley National Laboratory, Berkeley, CA, USA.

Zhou, Q., J. Bear, and J. Bensabat. 2005. Saltwater upconing and decay beneath a well pumping above an interface zone. *Transport in Porous Media* 61, no. 3: 337-363.

Zhou, Q., J.T. Birkholzer, C.F. Tsang, and J. Rutqvist. 2008. A method for quick assessment of CO_2 storage capacity in closed and semi-closed saline formations. *International Journal of Greenhouse Gas Control* 2, no. 4: 626-639.

Zhou, Q., J.T. Birkholzer, and C.F. Tsang. 2009. A semi-analytical solution for large-scale injection-induced pressure perturbation and leakage in a laterally bounded aquifer-aquitard system. *Transport in Porous Media* 78, no. 1: 127-148.

Table 1. Model parameters for the single-phase and two-phase flow in the five cases of sensitivity analysis

Case	Units	ϕ	k_h (10^{-15}m^2)	k_v (10^{-15}m^2)	β_p (10^{-10}Pa^{-1})	α^{-1} (10^5Pa)	m	S_{rb}	S_{rg}
A	EC	0.15	0.001	0.001	7.42	50.0	0.41	0.40	0.30
	CI_MS1	0.062-0.130	4.8-286	4.8-286	3.71	0.064–0.79	0.41	0.30	0.25
	CI_MS2	0.083-0.163	5.2-873	52-873	3.71	0.045–0.41	0.41	0.30	0.25
	CI_MS3	0.139-0.203	174-1000	174-1000	3.71	0.040	0.41	0.25	0.20
	CI_MS4	0.095	22.6	22.6	3.71	0.21	0.41	0.30	0.25
	NF_MS	0.12	100	100	3.71				
	FF_MS	0.16	500	500	3.71				
	PC	0.05	0.0001	0.0001	7.42	100.0	0.41	0.40	0.30
B	CI_MS1					0.50			
	CI_MS2					0.50			
C	CI_MS1		216	43		0.50			
	CI_MS2		216	43		0.50			
D	EC		0.0001	0.0001					
E	EC/PC				22.26				
	MS				11.13				

Note: EC for the Eau Claire Shale, MS for the Mt. Simon Sandstone, PC for the Precambrian granite, CI for the core injection area, NF for the near-field area, FF for the far-field area, and MSx for the Mt. Simon Unit number. Empty entries indicate not changed from Case A. ϕ is porosity, k_h is horizontal permeability, k_v is vertical permeability, β_p is pore compressibility, α^{-1} and m are two van Genuchten model parameters, representing the characteristic capillary pressure and pore-size distribution, respectively (van Genuchten 1980), S_{rb} is residual brine saturation, and S_{rg} is residual CO_2 saturation.

Figure 1. Overview of the Illinois Basin bounded by arches and domes, and the model domain: the flooded contour is the top elevation (m) of the Mt. Simon Sandstone, state borders are in thin black line, basin boundary in grey line, model boundary in red line, and faults or anticlines in thick black lines. Relevant to the scenario of full-scale GCS deployment are the core injection area outlined in white line, and the 20 injection sites in numbered black squares, as well as the ADM demonstration site in red square. Inset shows the location of the model domain.

Figure 2. Thickness of (a) the Mt. Simon Sandstone, (b) the Eau Claire Formation, (c) the upper unit of the Mt. Simon, and (d) the arkosic unit of the Mt. Simon. Also shown in (a) are the south-north and west-east cross sections, and the numbered eight observation points; shown in (c) are the data points in hollow circles for the division of the Mt. Simon into four units, and two key boreholes: the Weaber-Horn #1 and Hinton # 7 used for hydrogeologic property assignment in the core injection area.

Figure 3. Layer properties (in red line) of measured porosity, calculated permeability, and scaled characteristic capillary pressure for the 24 layers of the Mt. Simon and the Eau Claire and the Precambrian granite. Also shown is the division (in blue line) of the four hydrogeologic units of the Mt. Simon Sandstone, as well as the core-scale (0.15

m) porosity and permeability (in grey line) at the Weaber-Horn #1 well.

Figure 4. The two-dimensional mesh generated for the three-dimensional unstructured mesh, with higher resolution in the core injection area and around each injection center.

Figure 5. Contours of simulated CO_2 saturation along the south-north cross section at Storage Site 10, as a function of time, for Cases A, B, and C. Also shown in (a) is the distribution of log permeability (in background).

Figure 6. Contours of CO_2 saturation at the top elements of Layer 11, with maximum lateral extent of the plumes simulated at 50, and 200 years in Case A.

Figure 7. Comparison, between Cases A and B, of (a) pore volumes of mobile and immobile CO_2 and the total pore volume affected by CO_2, and (b) the fractional mass of immobile, mobile, and dissolved CO_2, during the injection and post-injection periods.

Figure 8. Contours of pressure buildup (bar) at 0.5, 5, 50, and 100 years in Case A, and at 50 years in Cases D and E. Also shown in (a) is the Illinois counties (in red line) with heavy pumping records, and the eight counties (in grey flood) in the Chicago metro region where significant pumping-induced drawdown has been observed.

Figure 9. (a) Transient pressure buildup and (b) its time derivative at eight observation points along the south-north cross section, (c) pressure buildup at the 20 injection centers at 0.5, 5, 10, 30, and 50 years, and (d) correlation between pressure buildup and Mt. Simon thickness at injection centers at 0.5, 5, and 50 years simulated in Case A.

Figure 10. (a) Volumetric balance between the resident brine displaced by injected CO_2 and that stored in the storage formation by pore and brine compressibility, and leaked through the caprock, and flowing out of the model domain through lateral open boundaries, and (b) annual leakage rate of resident brine through caprock top in the far-field, near-field, and core injection areas, as well as in the entire model domain.

Figure 11. (a) Comparison of the CO_2 injection rate (not with specific years) to the annual groundwater pumping rate in the eight-county metro-Chicago region and the entire north-central Illinois, and (b) simulated drawdown (in bar) in 2005 induced by heavy pumping in northern Illinois and southeastern Wisconsin.

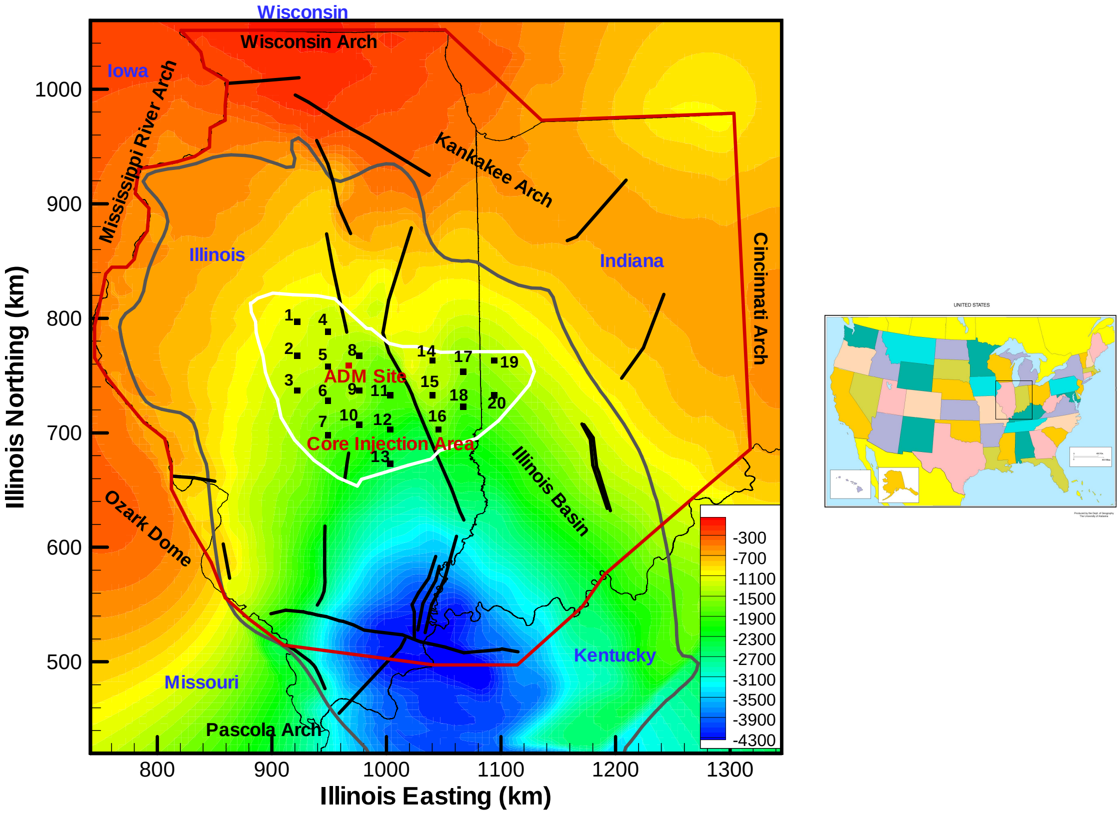

Wisconsin
Wisconsin Arch
Iowa
Mississippi River Arch
Kankakee Arch
Illinois
Indiana
Cincinnati Arch
1
2
3
4
5
6
7
8
9
10
11
12
13
14
15
16
17
18
19
20
ADM Site
Core Injection Area
Illinois Basin
Ozark Dome
Kentucky
Missouri
Pascola Arch
-300
-700
-1100
-1500
-1900
-2300
-2700
-3100
-3500
-3900
-4300
1000
900
800
700
600
500
Illinois Northing (km)
800
900
1000
1100
1200
1300
Illinois Easting (km)
UNITED STATES

Figure 1

(a) Mt Simon Thickness (m)

(b) Eau Claire Thickness (m)

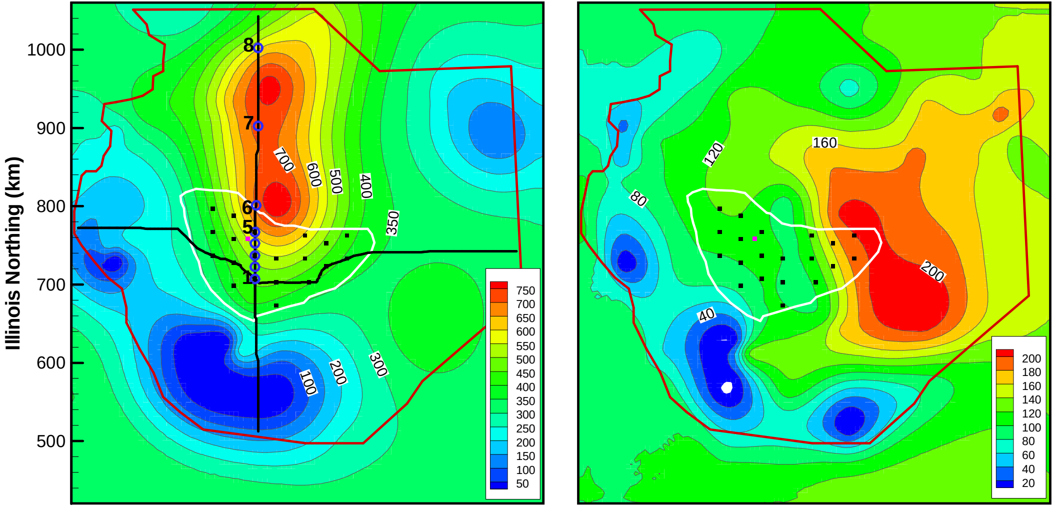

(c) Mt Simon Upper Unit Thickness (m)

(d) Mt Simon Arkosic Unit Thickness (m)

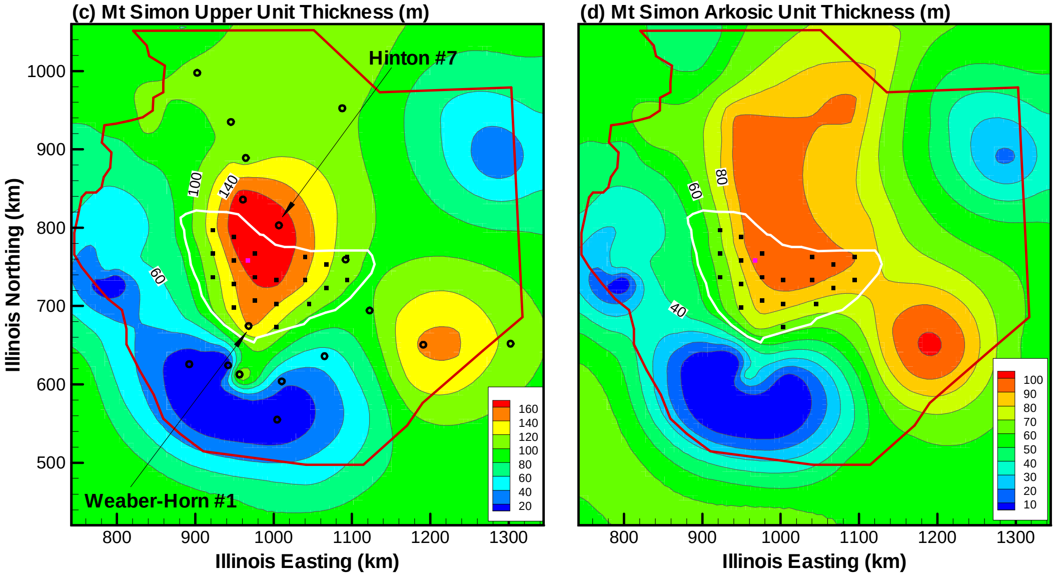

Figure 2.

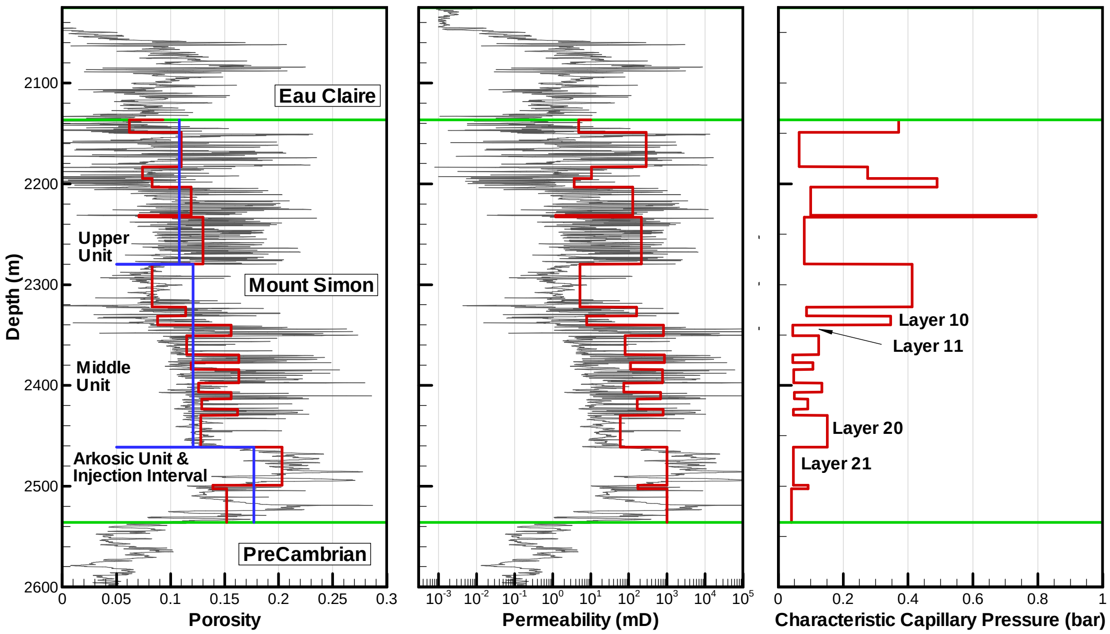

Figure 3.

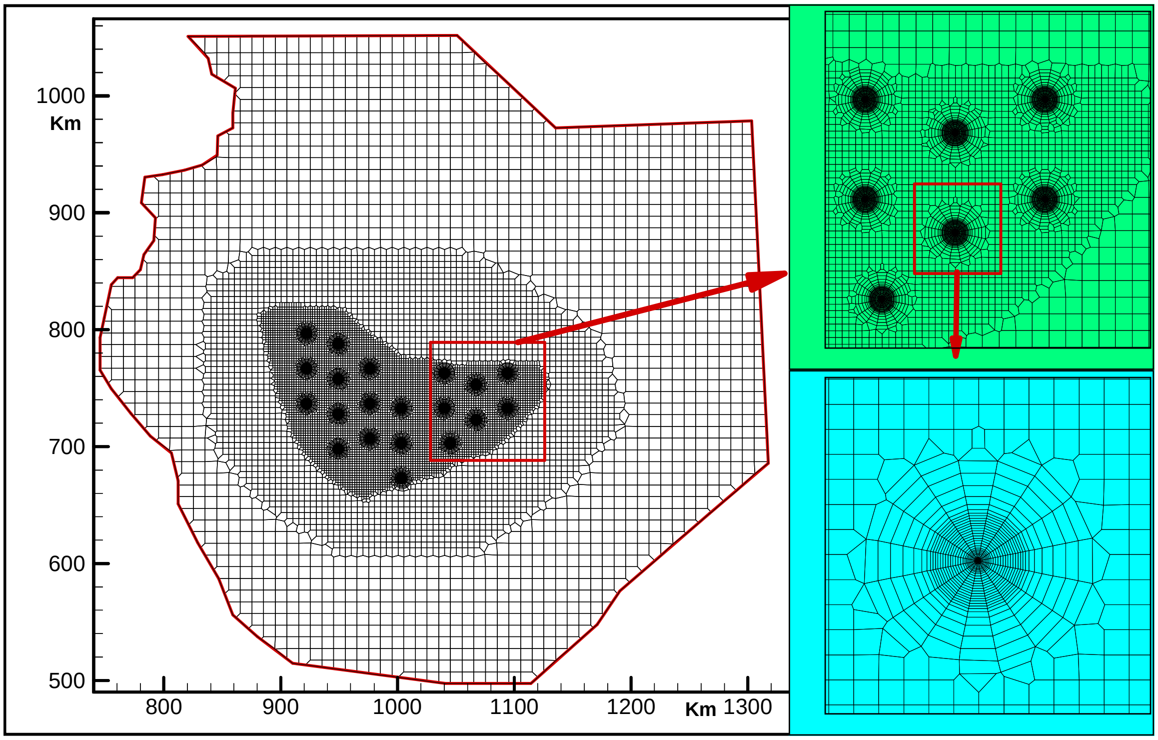

Figure 4.

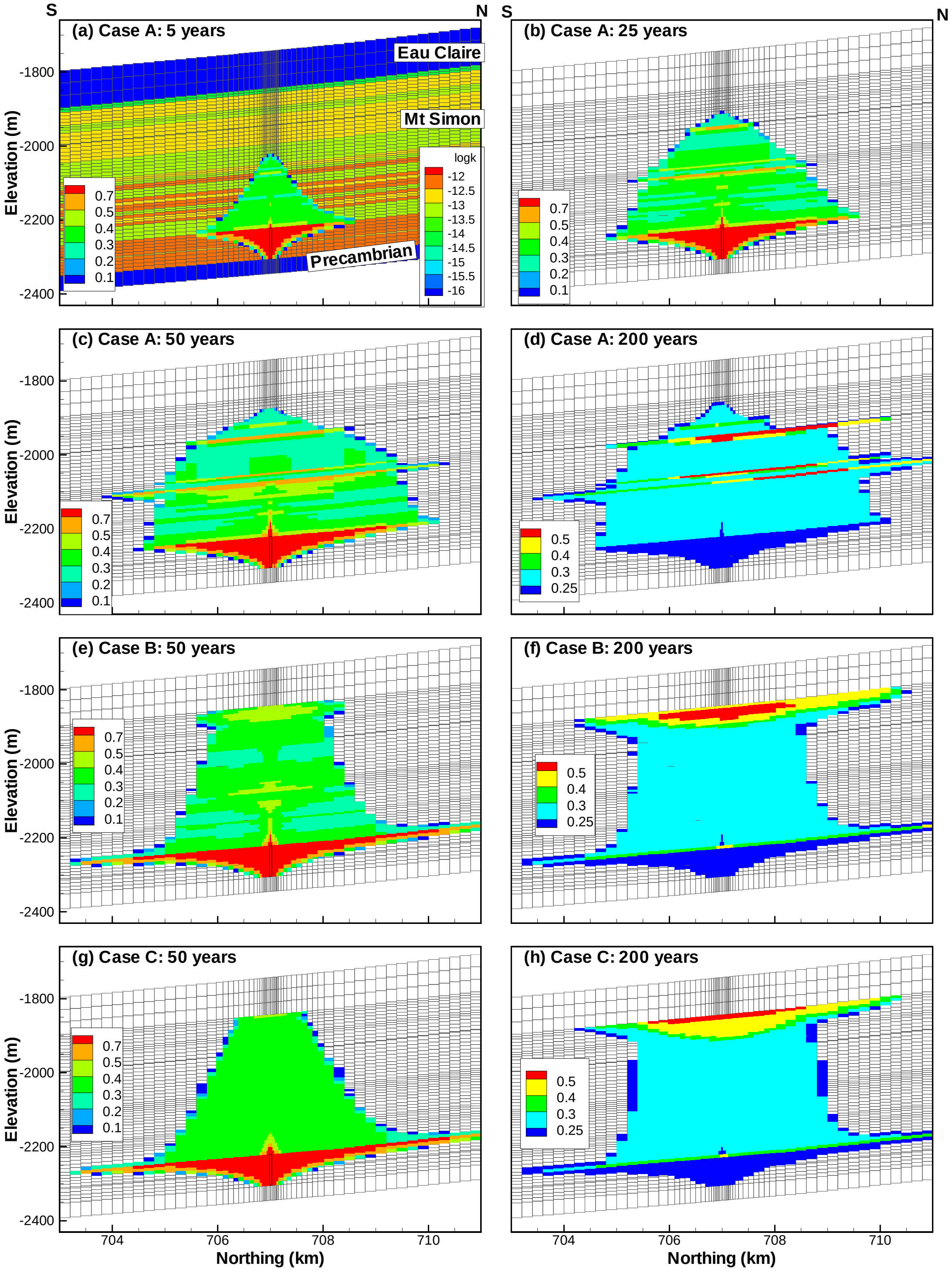
S
N
(a) Case A: 5 years
Eau Claire
Mt Simon
Precambrian
logk
-12
-12.5
-13
-13.5
-14
-14.5
-15
-15.5
-16
0.7
0.5
0.4
0.3
0.2
0.1
S
N
(b) Case A: 25 years
(c) Case A: 50 years
(d) Case A: 200 years
0.5
0.4
0.3
0.25
(e) Case B: 50 years
(f) Case B: 200 years
(g) Case C: 50 years
(h) Case C: 200 years
Elevation (m)
-1800
-2000
-2200
-2400
704
706
708
710
Northing (km)

Figure 5.

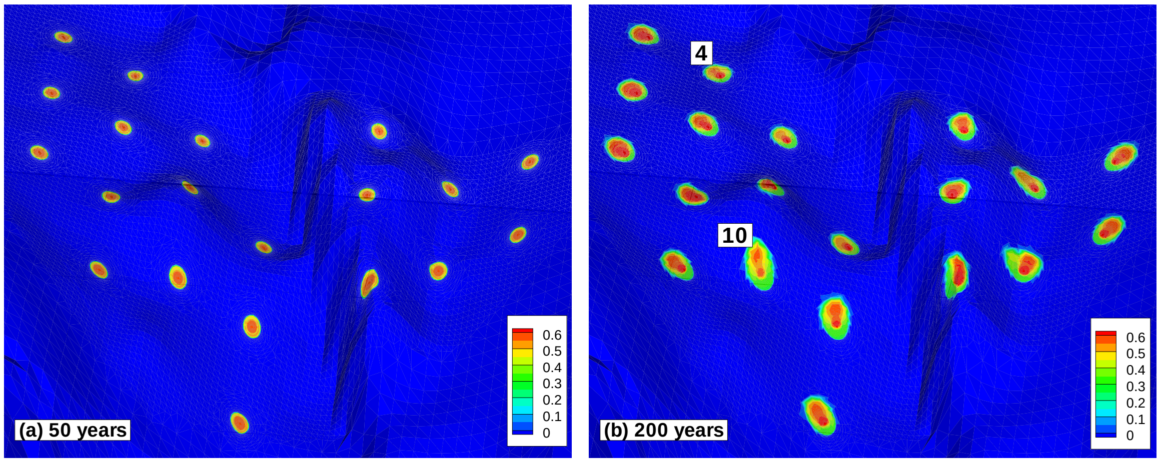

Figure 6.

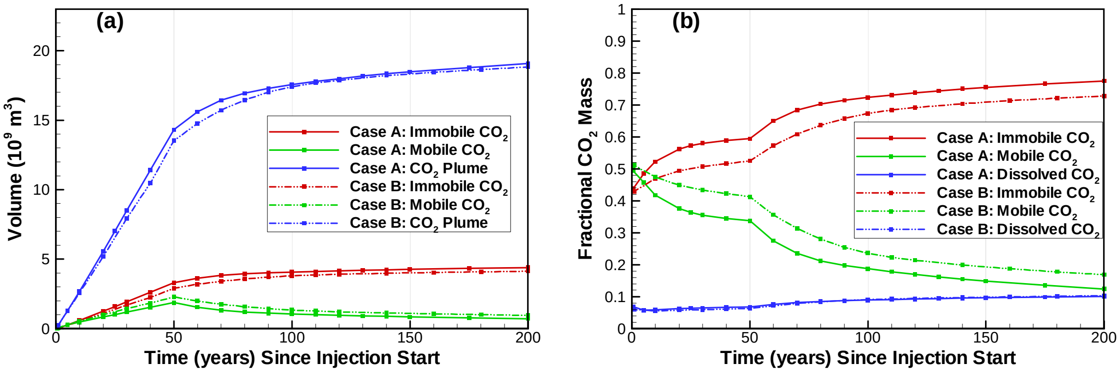

Figure 7.

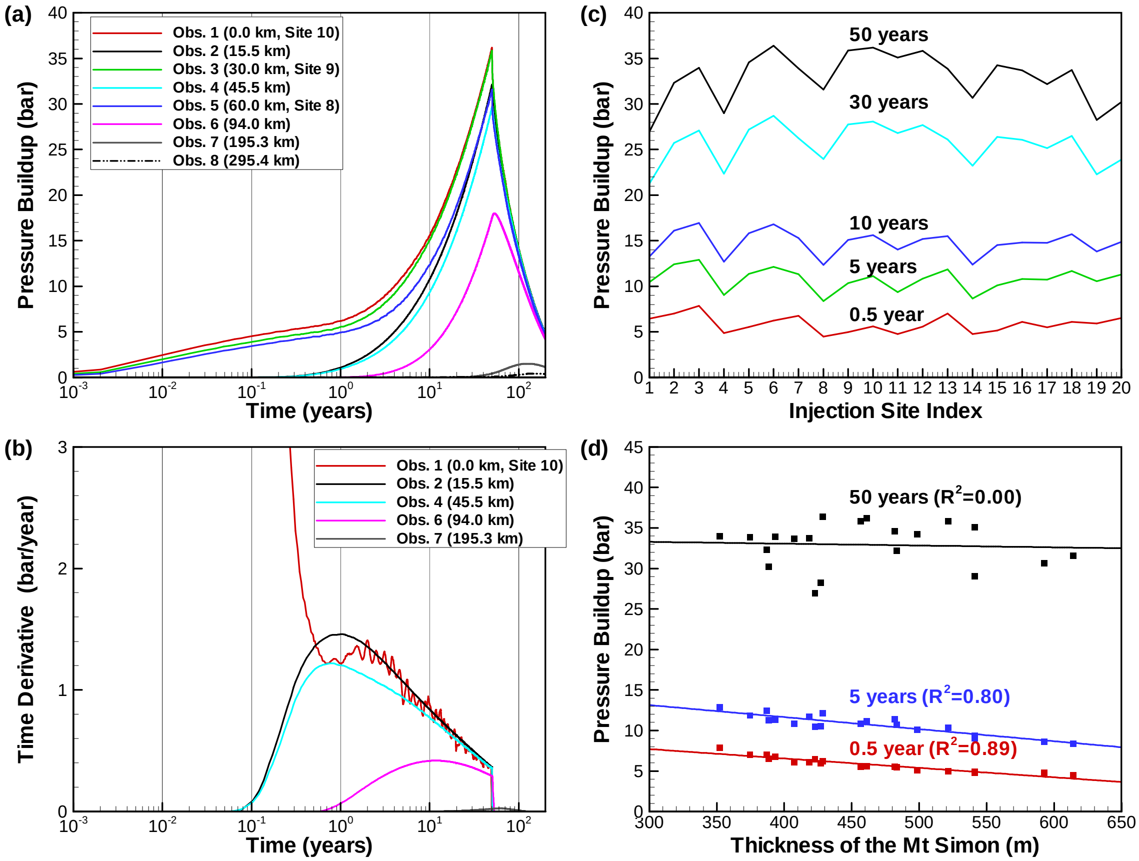
(a)
Pressure Buildup (bar)
Time (years)
Obs. 1 (0.0 km, Site 10)
Obs. 2 (15.5 km)
Obs. 3 (30.0 km, Site 9)
Obs. 4 (45.5 km)
Obs. 5 (60.0 km, Site 8)
Obs. 6 (94.0 km)
Obs. 7 (195.3 km)
Obs. 8 (295.4 km)
0
5
10
15
20
25
30
35
40
10^{-3}
10^{-2}
10^{-1}
10^{0}
10^{1}
10^{2}
(b)
Time Derivative (bar/year)
Time (years)
Obs. 1 (0.0 km, Site 10)
Obs. 2 (15.5 km)
Obs. 4 (45.5 km)
Obs. 6 (94.0 km)
Obs. 7 (195.3 km)
0
1
2
3
10^{-3}
10^{-2}
10^{-1}
10^{0}
10^{1}
10^{2}
(c)
Pressure Buildup (bar)
Injection Site Index
50 years
30 years
10 years
5 years
0.5 year
0
5
10
15
20
25
30
35
40
1
2
3
4
5
6
7
8
9
10
11
12
13
14
15
16
17
18
19
20
(d)
Pressure Buildup (bar)
Thickness of the Mt Simon (m)
50 years (R^2=0.00)
5 years (R^2=0.80)
0.5 year (R^2=0.89)
0
5
10
15
20
25
30
35
40
45
300
350
400
450
500
550
600
650

Figure 8.

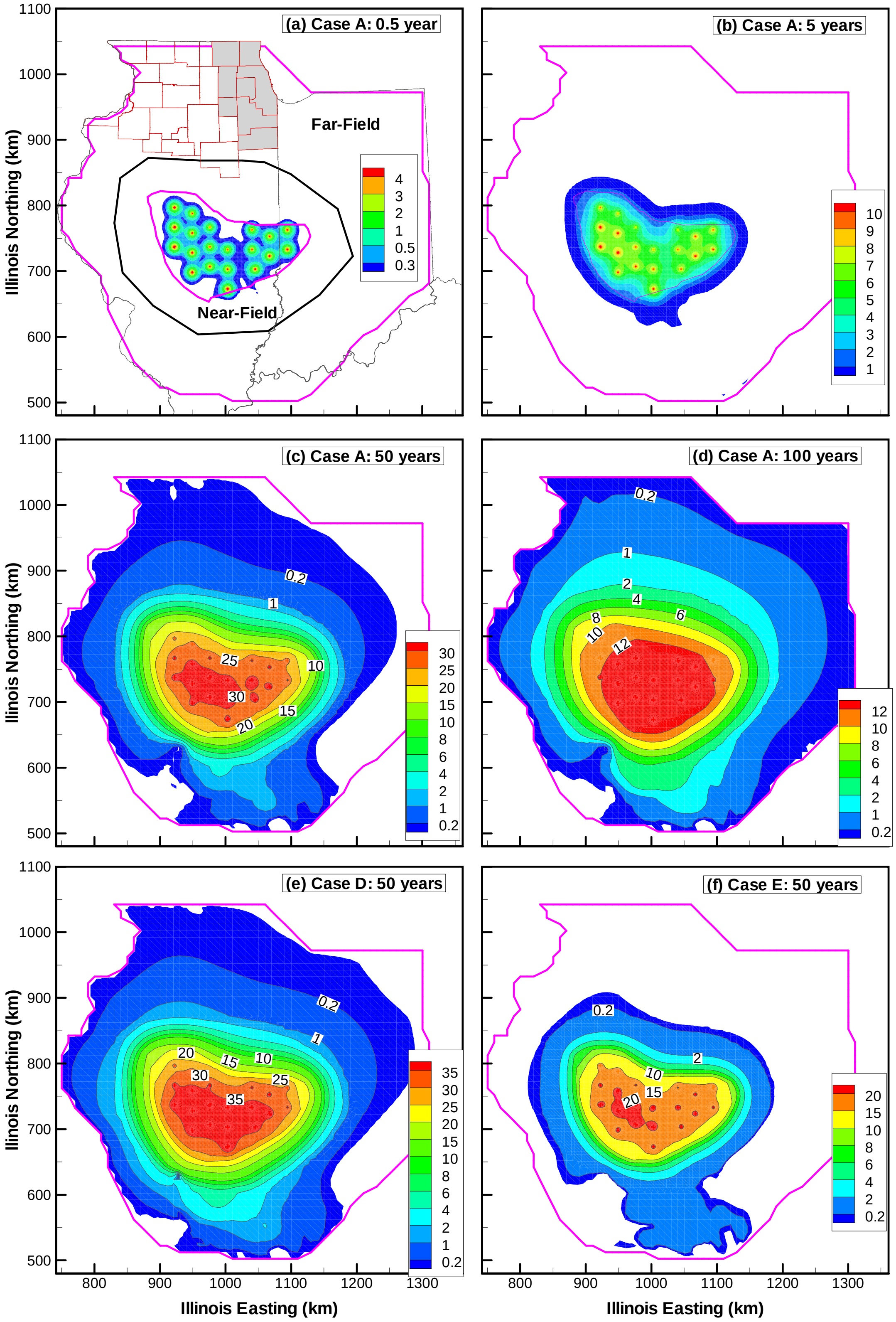
(a) Case A: 0.5 year
Far-Field
Near-Field
4
3
2
1
0.5
0.3
(b) Case A: 5 years
10
9
8
7
6
5
4
3
2
1
(c) Case A: 50 years
0.2
1
25
10
30
15
20
30
25
20
15
10
8
6
4
2
1
0.2
(d) Case A: 100 years
0.2
1
2
4
6
8
10
12
12
10
8
6
4
2
1
0.2
(e) Case D: 50 years
0.2
1
20
15
10
30
25
35
35
30
25
20
15
10
8
6
4
2
1
0.2
(f) Case E: 50 years
0.2
2
10
15
20
20
15
10
8
6
4
2
0.2
Illinois Northing (km)
1100
1000
900
800
700
600
500
Illinois Easting (km)
800
900
1000
1100
1200
1300

Figure 9.

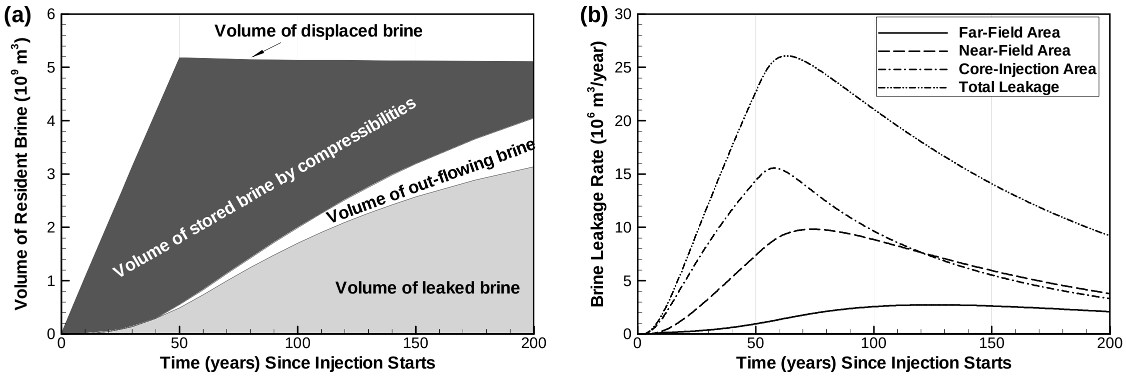

Figure 10.

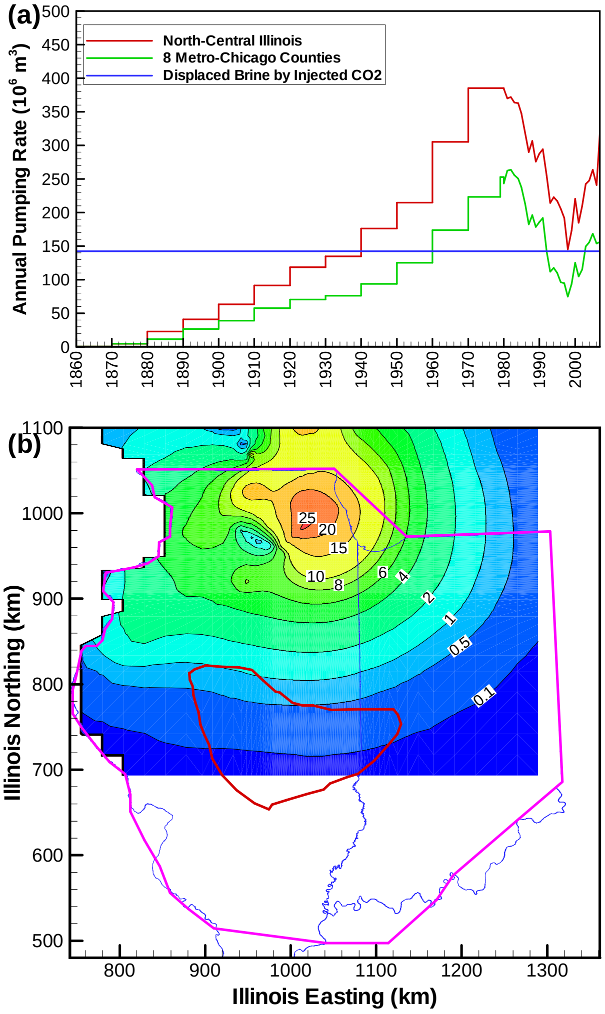

Figure 11.